frontiers | Frontiers in Environmental Chemistry

TYPE Original Research
PUBLISHED 26 September 2024
DOI 10.3389/fenvc.2024.1445482

OPEN ACCESS

EDITED BY
Sabine Neusatz Guilhen,
Instituto de Pesquisas Energéticas e Nucleares (IPEN), Brazil

REVIEWED BY
Károly Lázár,
Eötvös Loránd Research Network, Hungary
Mícheál P. Moloney,
Université de Montpellier, France

*CORRESPONDENCE
Azusa Ito,
ito.azusa@jaea.go.jp
Joseph A. Hriljac,
joe.hriljac.vis@diamond.ac.uk

†These authors have contributed equally to this work

RECEIVED 07 June 2024
ACCEPTED 14 August 2024
PUBLISHED 26 September 2024

CITATION
Ito A, Thirunavukkarasu G and Hriljac JA (2024) Superparamagnetically modified A-type, X-type and CHA-type zeolites with silica-coated Fe_3O_4 and $CoFe_2O_4$ nanoparticles for removal of Sr^{2+} and Cs^+ from radioactively contaminated water. *Front. Environ. Chem.* 5:1445482. doi: 10.3389/fenvc.2024.1445482

Superparamagnetically modified A-type, X-type and CHA-type zeolites with silica-coated Fe_3O_4 and $CoFe_2O_4$ nanoparticles for removal of Sr^{2+} and Cs^+ from radioactively contaminated water

Azusa Ito[1,2*†], Gnanavel Thirunavukkarasu[3] and Joseph A. Hriljac[1,4*†]

[1]School of Chemistry, University of Birmingham, Birmingham, United Kingdom, [2]Japan Atomic Energy Agency, Collaborative Laboratories for Advanced Decommissioning Science (CLADS), Waste Stream Research Group, Tokai-Mura, Japan, [3]School of Metallurgy and Materials, University of Birmingham, Birmingham, United Kingdom, [4]Diamond Light Source Ltd., Harwell Science and Innovation Campus, Didcot, United Kingdom

Magnetised zeolite A, zeolite X and Na,K-CHA composites with superparamagnetic nanoparticles of SiO_2-coated Fe_3O_4 or $CoFe_2O_4$ ferrite spinels were prepared, characterised and tested for ion exchange efficacy. They were synthesised by following three steps, synthesising Fe_3O_4 and $CoFe_2O_4$ nanoparticles by a solvothermal method, coating the metal oxide particles with SiO_2 by a sol-gel process, and attaching the M_xO_y/SiO_2 onto the zeolites during synthesis. The magnetic zeolites were characterised by X-ray diffraction, X-ray fluorescence spectroscopy, Raman spectroscopy, vibrating sample magnetometry and both scanning and transmission electron microscopy. It was confirmed they had superparamagnetic properties due to successful attachment of the M_xO_y/SiO_2 particles onto the zeolites. Adsorption capacities of Sr^{2+} onto the magnetic zeolite A and zeolite X and Cs^+ onto the magnetic Na,K-CHA were also evaluated. The results show the M_xO_y/SiO_2 did not block the adsorption sites of the zeolites and the M_xO_y/SiO_2 particles were not detached from the zeolites during the adsorption experiments.

KEYWORDS

zeolite, ion exchange, magnetic separation, superparamagnetism, Cs removal, Sr removal

1 Introduction

Sr-90 and Cs-137 are common fission products from U-235 nuclear fuels, and they adversely affect human bodies due to their radioactivity (beta and gamma emitters, respectively) and long half-lives (28.91 and 30.08 years, respectively) (Browne and Tuli, 2007; Basu and McCutchan, 2020). Generally, the radionuclides are released during fuel reprocessing into liquid effluents, furthermore, a large amount of the radionuclides have also been released into cooling water used for the reactor cores damaged by the TEPCO Fukushima Daichi accident in Japan. For radioactively contaminated water remediation, chemical coprecipitation and adsorptive separation methods have both been studied, such

TABLE 1 Initial pH, and Sr and Cs concentrations used for the pH-dependent studies.

M_xO_y/SiO_2/zeolite A, M_xO_y/SiO_2/zeolite X		M_xO_y/SiO_2/Na,K-CHA	
pH	Sr (mg/L)	pH	Cs (mg/L)
4.06	129 ± 3	4.04	107 ± 2
7.00	131 ± 4	6.89	99 ± 5
9.96	112 ± 3	10.03	96 ± 2

as carbonate coprecipitation of Sr-90 and adsorption of both cations by monosodium titanate, sodium silicotitanate (commercially available as IONSIV™ IE-911), hydroxyapatite, bentonite, and zeolites (Sugihara et al., 1959; Oji et al., 2009; Nishiyama et al., 2016; Kubota et al., 2013). After the remediation process, the coprecipitation sludge and spent adsorbents are normally immobilised in cement, polymers or geopolymers and disposed of as low or intermediate level radioactive wastes (International atomic energy agency, 2001; Lichvar et al., 2013). Aluminosilicate zeolites can effectively remove Sr^{2+} and Cs^{+} from aqueous solutions by cation-exchanging with Na^{+}, examples are zeolites Na-A and Na-X for Sr^{2+} and Na,K-chabazite (CHA) for Cs^{+} (Mimura and Kanno, 1985; Munthali et al., 2015). Commonly, zeolite monoliths, beads, or pellets are packed in a filtration column for the water remediation, such as the KURION system used at TEPCO Fukushima Daiichi (Hijikata et al., 2014), because the zeolite can then be easily replaced, however, the system has less cation-exchange efficiency than suspending zeolite particles directly in the water due to the lower surface contact area and time. Contaminated water sources can cover a range of pH values, some are low due to acid decontamination solutions, ground water is typically in the range of pH 6 to 8.5 and base-stabilized solutions can be over pH 10. Hence, materials are typically tested over a range of pH values to assess applicability.

Magnetically modified zeolites (MZ), such as one with attached metal oxide particles that can be collected by an external magnetic field, have been proposed to improve the water remediation process and efficiency. For example, Faghihian et al. have studied a superparamagnetic zeolite A nanocomposite for Sr^{2+} and Cs^{+} removal, the nanocomposite was synthesised by co-precipitation of nano-sized Fe_3O_4 on pre-synthesised zeolite A in an aqueous Fe (II)/Fe (III) solution (Faghihian et al., 2014). It exhibited a high magnetisation (up to 19.03 emu/g at about 9 kOe), but Sr^{2+} and Cs^{+} capacities of the nanocomposite were decreased as the Fe_3O_4 to zeolite A ratio increased. A one-pot synthesis method is another way to synthesise a MZ, nano-sized Fe_3O_4 or $CoFe_2O_4$ were formed solvothermally on Na,K-CHA particles from Fe (III) and/or Co (II) acetylacetonate and 1-hexanol (Ito et al., 2023). The Cs^{+} adsorption isotherms of both Fe_3O_4/Na,K-CHA and $CoFe_2O_4$/Na,K-CHA were almost the same as pure Na,K-CHA, and they could also be separated by a neodymium magnet from aqueous solutions, even though the maximum magnetizations were less than 6.3 emu/g at 50 kOe. In both papers, the authors reported the metal oxide particles were observed on the surface of the zeolite particles. Fe_3O_4 can transform to γ-Fe_2O_3, α-FeOOH and α-Fe_2O_3 by water, humid air, or heating (Meisel, 1998). $CoFe_2O_4$ is not degraded under the same conditions, however, both Fe_3O_4 and

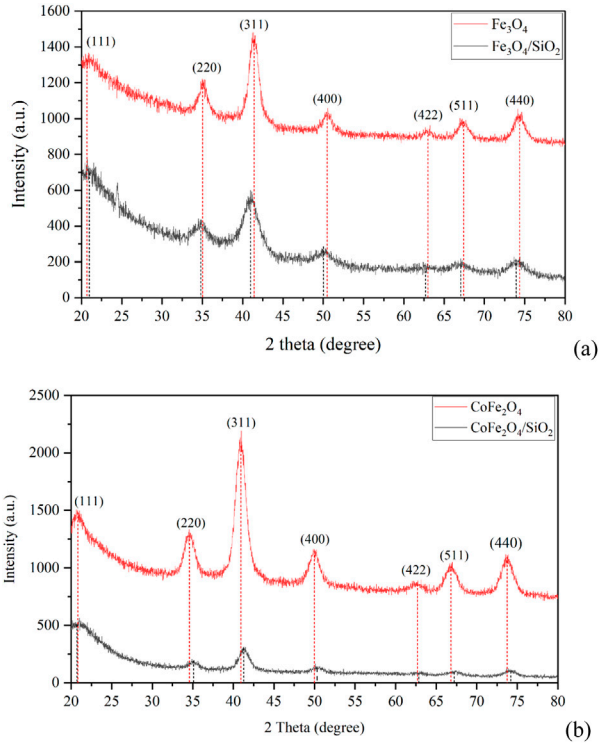

FIGURE 1
XRD patterns of **(A)** Fe_3O_4 and Fe_3O_4/SiO_2 and **(B)** $CoFe_2O_4$ and $CoFe_2O_4/SiO_2$ with positions from fitting individual peaks denoted by vertical lines.

$CoFe_2O_4$ are harmful due to the particle sizes if they are detached from the zeolite surfaces. Therefore, we have investigated a new type of MZ where silica-coated Fe_3O_4 or $CoFe_2O_4$ were attached onto zeolite particles (M_xO_y/SiO_2/zeolite).

A SiO_2 coating is commonly used to protect M_xO_y particles, this is applied using a synthesis method that creates size controlled monodisperse SiO_2-coated particles by a sol-gel reaction of tetra-alkyl silicates with an aqueous ethanol and ammonia solution (Stöber et al., 1968). Ideally, thinner SiO_2 layers on M_xO_y particles are preferred to avoid a decrease in magnetisation. The SiO_2 thickness can be controlled by adjusting several aspects including the ratio of the tetra-alkyl silicate source and ethanol, the pH of the reaction medium, the reaction temperature and time. Dang, et al. investigated how these factors affect the SiO_2 thickness on Fe_3O_4 particles and the particle aggregation (Dang et al., 2010). The SiO_2 layer became thicker as the reaction temperature and pH of the reaction medium (over pH 10.5)

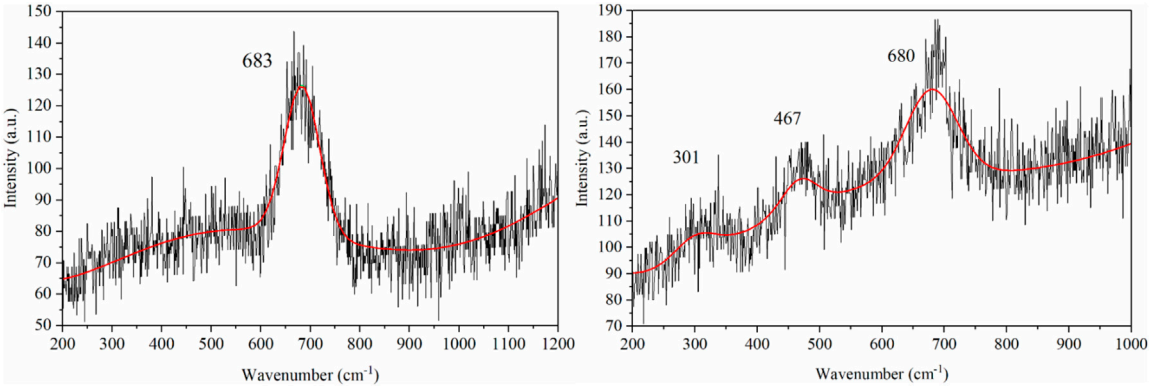

FIGURE 2
Raman spectra of Fe_3O_4 (left) and $CoFe_2O_4$ (right).

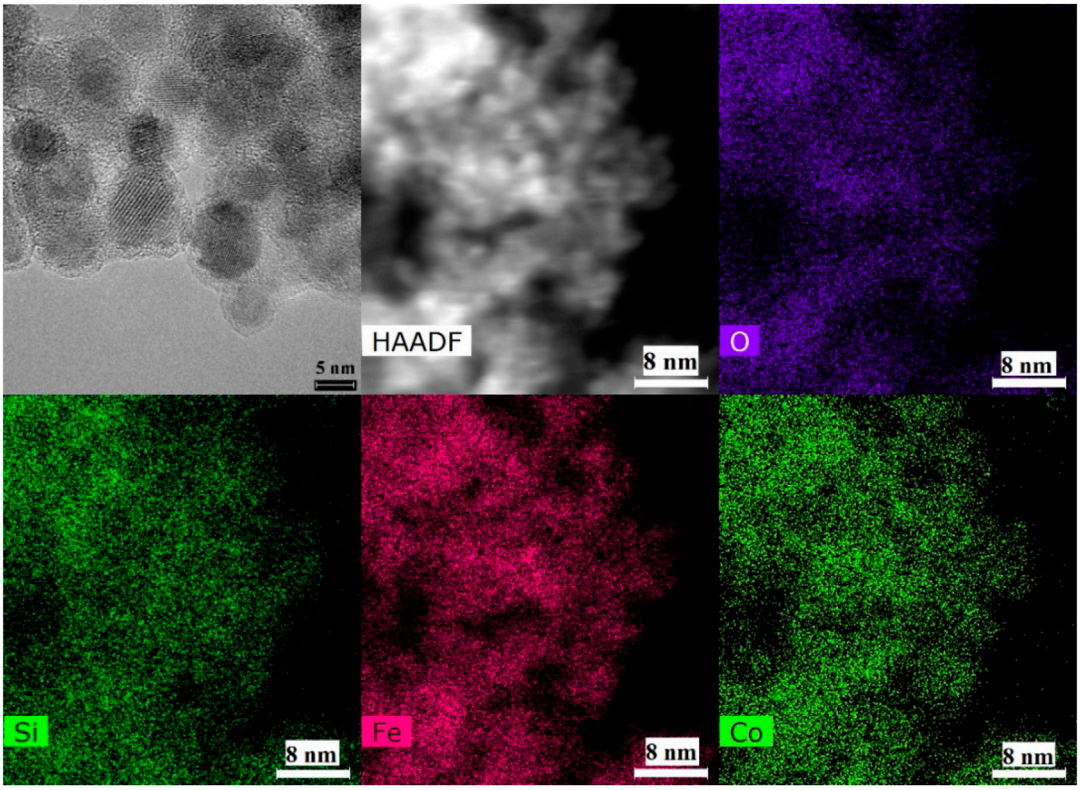

FIGURE 3
TEM images and EDS mapping of $CoFe_2O_4/SiO_2$ particles.

increased, and the authors assumed there were ideal values of the pH and the ethanol concentration in the reaction medium to avoid the particle agglomeration. Agglomerated Fe_3O_4/SiO_2 particles were formed when both ethanol concentration and pH in the reaction medium were high as well as when they are low. On the other hand, the reaction time was longer when the reaction temperature was decreased, and the Fe_3O_4 was uncoated in pH 8 medium.

In this study, the Fe_3O_4/SiO_2 or $CoFe_2O_4/SiO_2$ particles attached to zeolite A, zeolite X and Na,K-CHA were synthesised by three steps: (Browne and Tuli, 2007): synthesis of nano-sized Fe_3O_4 or $CoFe_2O_4$, (Basu and McCutchan, 2020), formation of a thin SiO_2 coating on the Fe_3O_4 or $CoFe_2O_4$ particles, and (Sugihara et al., 1959) incorporating the Fe_3O_4/SiO_2 or $CoFe_2O_4/SiO_2$ particles in the zeolite by mixing them into the zeolite synthesis process. Then, the morphology, magnetisation and Cs or Sr exchange characteristics were evaluated, and the results were compared with the M_xO_y/Na,K-CHA to evaluate how the SiO_2 coatings affect the magnetisation and cation exchange abilities.

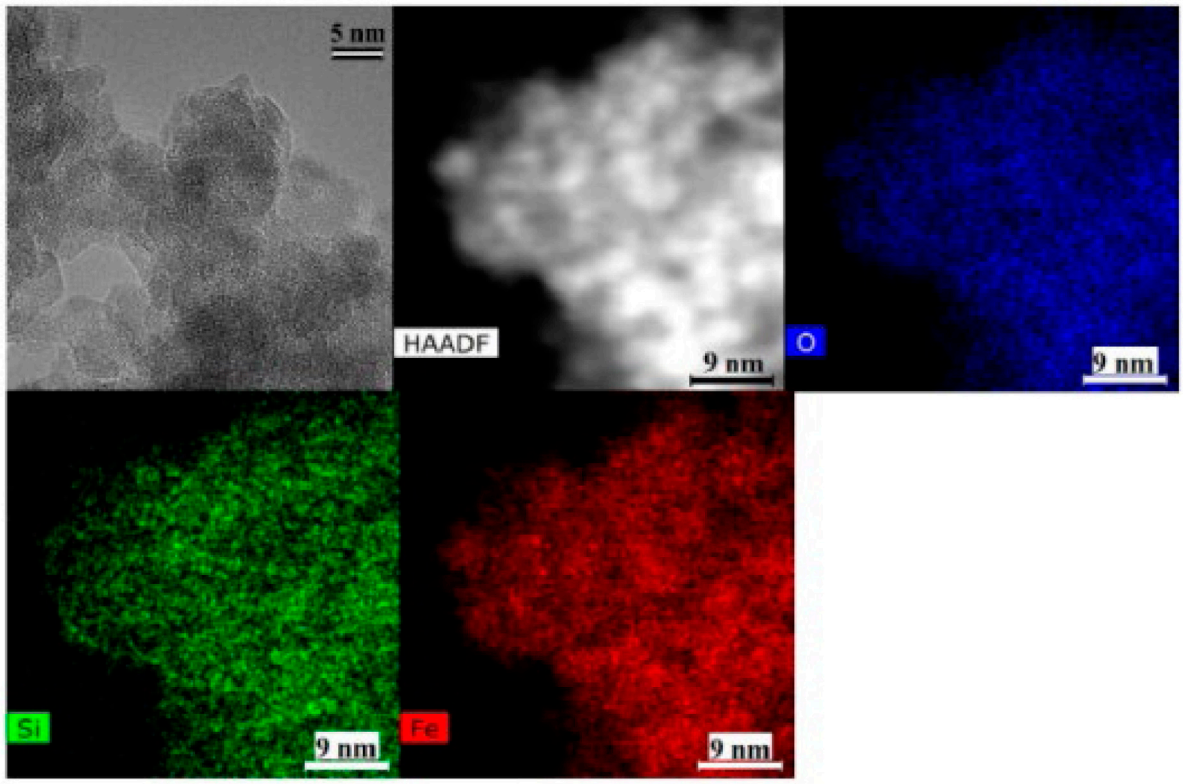

FIGURE 4
TEM images and EDS mapping of Fe_3O_4/SiO_2 particles.

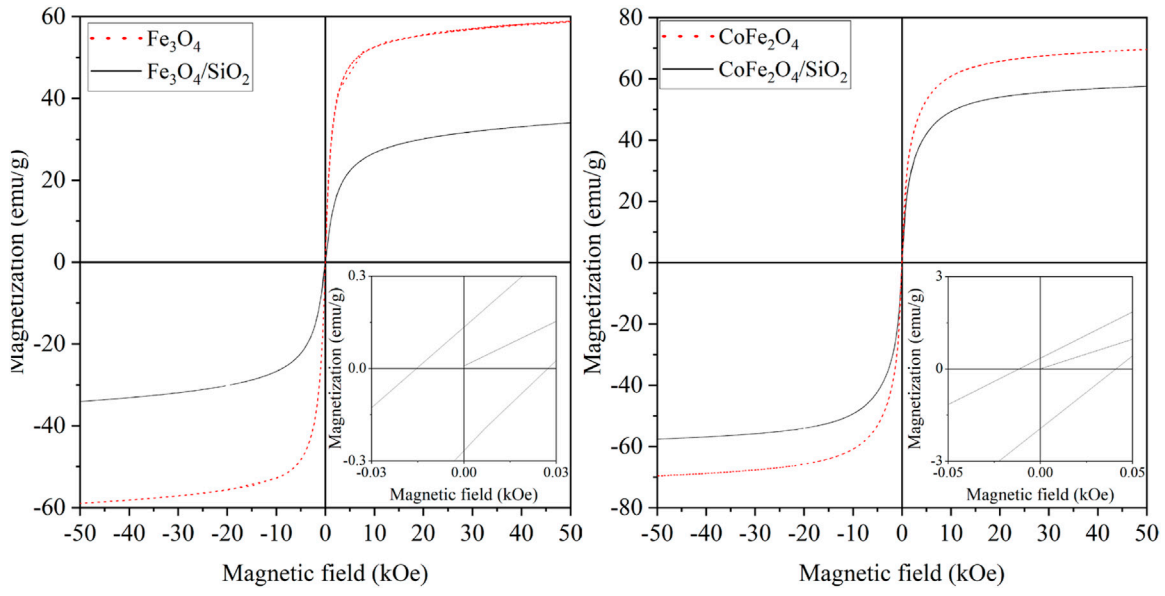

FIGURE 5
Magnetisation curves of Fe_3O_4 and Fe_3O_4/SiO_2 (left), and $CoFe_2O_4$ and $CoFe_2O_4/SiO_2$ (right) at 300 K.

TABLE 2 Derived magnetic properties of Fe_3O_4, Fe_3O_4/SiO_2, $CoFe_2O_4$ and $CoFe_2O_4/SiO_2$ at 300 K (H_c is the coercive field, M_s is the saturation magnetisation, and M_r is the remnant magnetisation).

	H_c	M_s	M_r	M_r/M_s
Fe_3O_4	−0.002	58.916	0.320	0.005
	0.008	−58.978	−0.338	0.006
Fe_3O_4/SiO_2	−0.015	34.051	0.130	0.004
	0.028	−34.062	−0.132	0.004
$CoFe_2O_4$	−0.023	69.600	0.840	0.012
	−0.012	69.600	0.330	−0.005
$CoFe_2O_4/SiO_2$	−0.011	57.601	0.350	0.006
	0.042	−57.602	−1.950	0.034

2 Experimental details

2.1 Materials

For the syntheses of Fe_3O_4 and $CoFe_2O_4$ nanoparticles, iron (III) acetylacetonate [97% Fe $(acac)_3$, Sigma-Aldrich] and/or cobalt (II) acetylacetonate [97% Co $(acac)_2$, Sigma-Aldrich], 1-hexanol (>99%, Sigma-Aldrich), ethanol (>99.8%, Fisher Chemical) and dichloromethane (99.8%, DCM, Sigma-Aldrich) were used.

For the Fe_3O_4/SiO_2 and $CoFe_2O_4/SiO_2$ syntheses, ethanol, ammonia hydroxide (28% NH_3, Fisher Chemical), tetraethyl orthosilicate (≥99.0%, TEOS, Sigma-Aldrich) and deionized water (DI water), were used.

For the Fe_3O_4/SiO_2/zeolite A and $CoFe_2O_4/SiO_2$/zeolite A syntheses, NaOH (Fisher Chemical), sodium aluminate (Technical, Fisher Chemical), sodium metasilicate pentahydrate (Technical, Fisher Chemical) and DI water were used.

For the Fe_3O_4/SiO_2/zeolite X and $CoFe_2O_4/SiO_2$/zeolite X syntheses, sodium aluminate, sodium metasilicate pentahydrate (Technical, Fisher Chemical) and DI water were used.

For the Fe_3O_4/SiO_2/Na,K-CHA and $CoFe_2O_4/SiO_2$/Na,K-CHA syntheses, the ammonium form of zeolite Y (Alfa Aesar), 45% KOH solution (Honywell Fluka), NaCl (Fisher Chemical) and DI water were used.

For the Cs and Sr adsorption experiments, $CsNO_3$ (99.99% Sigma-Aldrich), $Sr(NO_3)_2$ (99.97%, Alfer Aesar), ultrapure 2% HNO_3 solution, 1,000 mg/L $CsNO_3$ ICP standard (Merck Millipore), 1,000 mg/L $Sr(NO_3)_2$ ICP standard (Merck Millipore), 1,000 mg/L $RbNO_3$ (Merk Millipore), 1,000 mg/L $Y(NO_3)_3$ (Merk Millipore), 2-[4t-(2-hydroxyethl)piperazin-1-yl]ethanesulfonic acid (>99.5% HEPES, Sigma-Aldrich), N-cyclohexyl-3-aminopropanesulfonic acid (>99% CAPS, Sigma-Aldrich) and ultrapure water were used.

2.2 Synthesis of M_xO_y nanoparticles

The Fe_3O_4 and $CoFe_2O_4$ nanoparticles were prepared by the same synthesis method described by Ito et al. (Ito et al., 2023). In a glovebox under argon, a glass liner for a Teflon-lined 45 mL autoclave was charged with either 2.00 g (5.7 mmol) of Fe $(acac)_3$ and 20 mL of 1-hexanol or 1.70 g (4.8 mmol) of Fe $(acac)_3$, 0.62 g (2.4 mmol) of Co$(acac)_2$ and 20 mL of 1-hexanol. Additionally, 5 mL of 1-hexanol was filled between the glass liner and the Teflon liner to prevent an overflow of the reagents. The autoclave was heated in a conventional oven at 175°C for 5 h for Fe_3O_4 or at 180°C for 10 h for $CoFe_2O_4$. The products were collected by centrifugation at 11,000 rpm for 10 min, and then washed with ethanol and DCM each three times. After each washing, they were collected by centrifugations under the same condition, and the final washed particles were dried at 60°C. Typical yields were 0.18 g of Fe_3O_4 and 0.41 g of $CoFe_2O_4$.

2.3 Synthesis of M_xO_y/SiO_2 nanoparticles

50 mL of DI water and 200 mL of ethanol were charged in a 500 mL short neck boiling flask. The pH of the solvent was adjusted to about 10.50 with 28% NH_3 solution. It was degassed by N_2 for 10 min, and then 0.25 g of Fe_3O_4 or $CoFe_2O_4$ nanoparticles were dispersed in the solvent using an ultrasonic bath (40 kHz) for 10 min. Either 2.00 mL of TEOS for Fe_3O_4/SiO_2 or 1.00 mL of TEOS for $CoFe_2O_4/SiO_2$ was added in the solvent mixture, and it was ultrasonicated for 2 h. The ultrasonic bath temperature was controlled to between about 20°C and 30°C. The products were collected by centrifugation at 11,000 rpm for 10 min, and then were washed with ethanol and collected by centrifugation under the same conditions three times. The final washed particles were dried at 60°C. Typical yields were 0.17 g of Fe_3O_4/SiO_2 and 0.21 g of $CoFe_2O_4/SiO_2$.

2.4 Synthesis of M_xO_y/SiO_2/zeolite

The zeolite A, zeolite X and Na,K-CHA were synthesised by following the recipes of Robson (Robson, 2001). Firstly, either zeolite A or zeolite X seed gel were synthesised.

For the synthesis of the zeolite A seed gel, 0.22 g of NaOH was dissolved in 2.4 mL of DI water, then the solution was divided into two. Into one of the solutions 0.25 g of sodium aluminate was dissolved and into the other 0.47 g of sodium metasilicate pentahydrate. These solutions were combined slowly, and the mixture was shaken by a vortex mixier for 1 h.

For the synthesis of the zeolite X seed gel, two solutions were prepared first, 0.68 g of sodium metasilicate pentahydrate was dissolved in 1.5 mL of DI water, and 0.22 g sodium aluminate was dissolved in 1.0 mL of DI water. These solutions were combined slowly, and the mixture was also shaken by a vortex mixier for 1 h.

For the syntheses of M_xO_y/SiO_2/zeolite A or M_xO_y/SiO_2/zeolite X, 0.1 g of either the Fe_3O_4/SiO_2 or the $CoFe_2O_4/SiO_2$ were mixed with either the zeolite A seed gel or the zeolite X seed gel, and the mixtures were shaken by the vortex mixer for 1 h. Then, the mixtures were heated in a rotation oven at 99°C for 5 h for M_xO_y/SiO_2/zeolite A or 90°C for 24 h for M_xO_y/SiO_2/zeolite X. The final products were collected by the centrifugation at 4,400 rpm for 5 min, and then washed with DI water and collected by centrifugation under the same conditions three times. The final washed particles were dried at 60°C. The

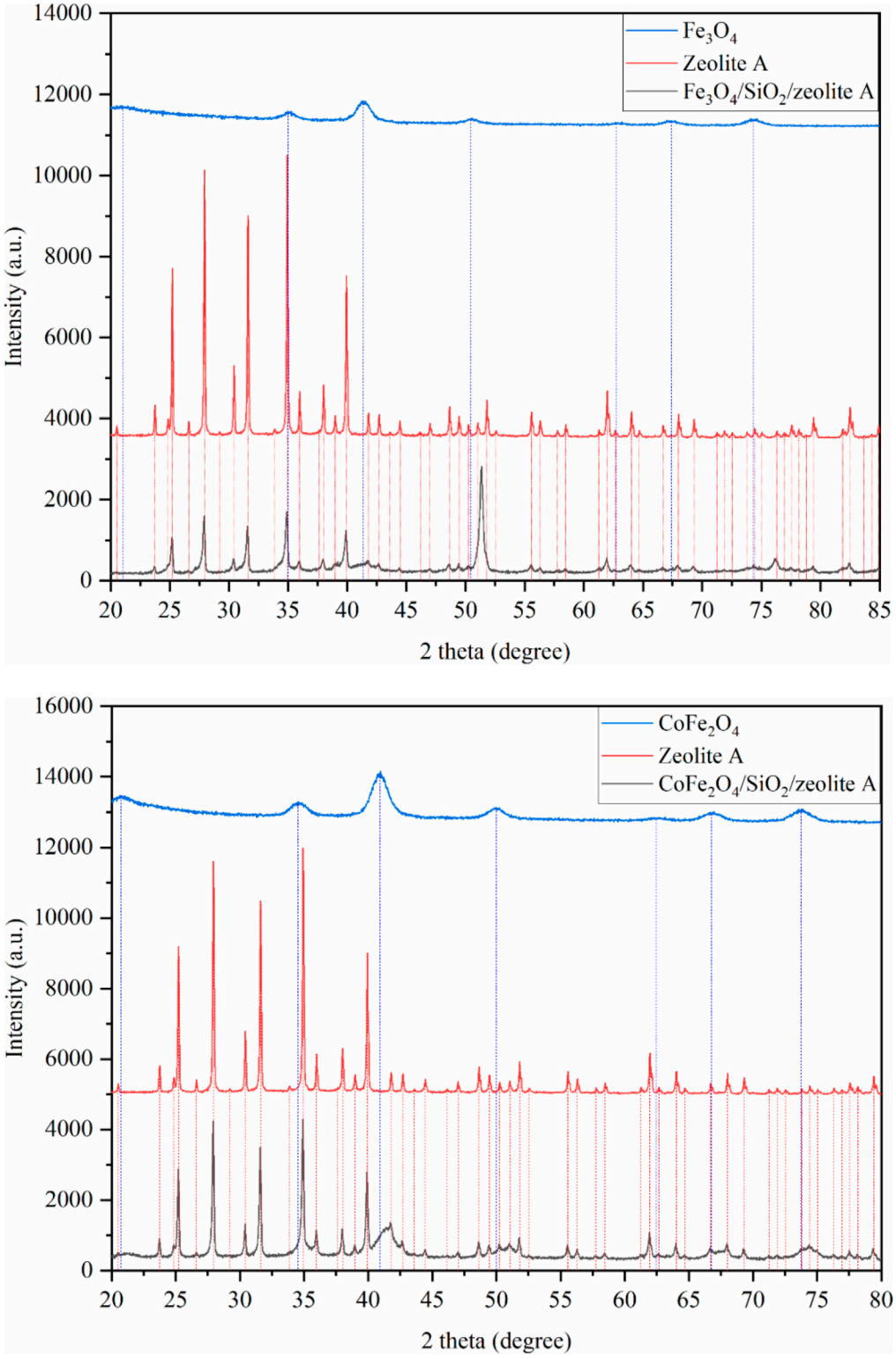

FIGURE 6
XRD patterns of Fe_3O_4/SiO_2/zeolite A (top) and $CoFe_2O_4/SiO_2$/zeolite A (bottom). The vertical lines are peak positions from individual fits.

synthesised M_xO_y/SiO_2/zeolites contained ca. 23%–25% of M_xO_y/SiO_2.

For the synthesis of M_xO_y/SiO_2/Na,K-CHA, firstly, the ammonium form of zeolite Y was calcined in a furnace at 550°C (the ramp rate was 2°C/min) for 2 h to change it to hydrogen form. A 0.36 g portion of zeolite H-Y was dispersed in 3.51 M KOH solution, and it was shaken by a vortex mixer for 1 h. A 0.1 g portion of either of the Fe_3O_4/SiO_2 or the $CoFe_2O_4/SiO_2$ was added and it was shaken

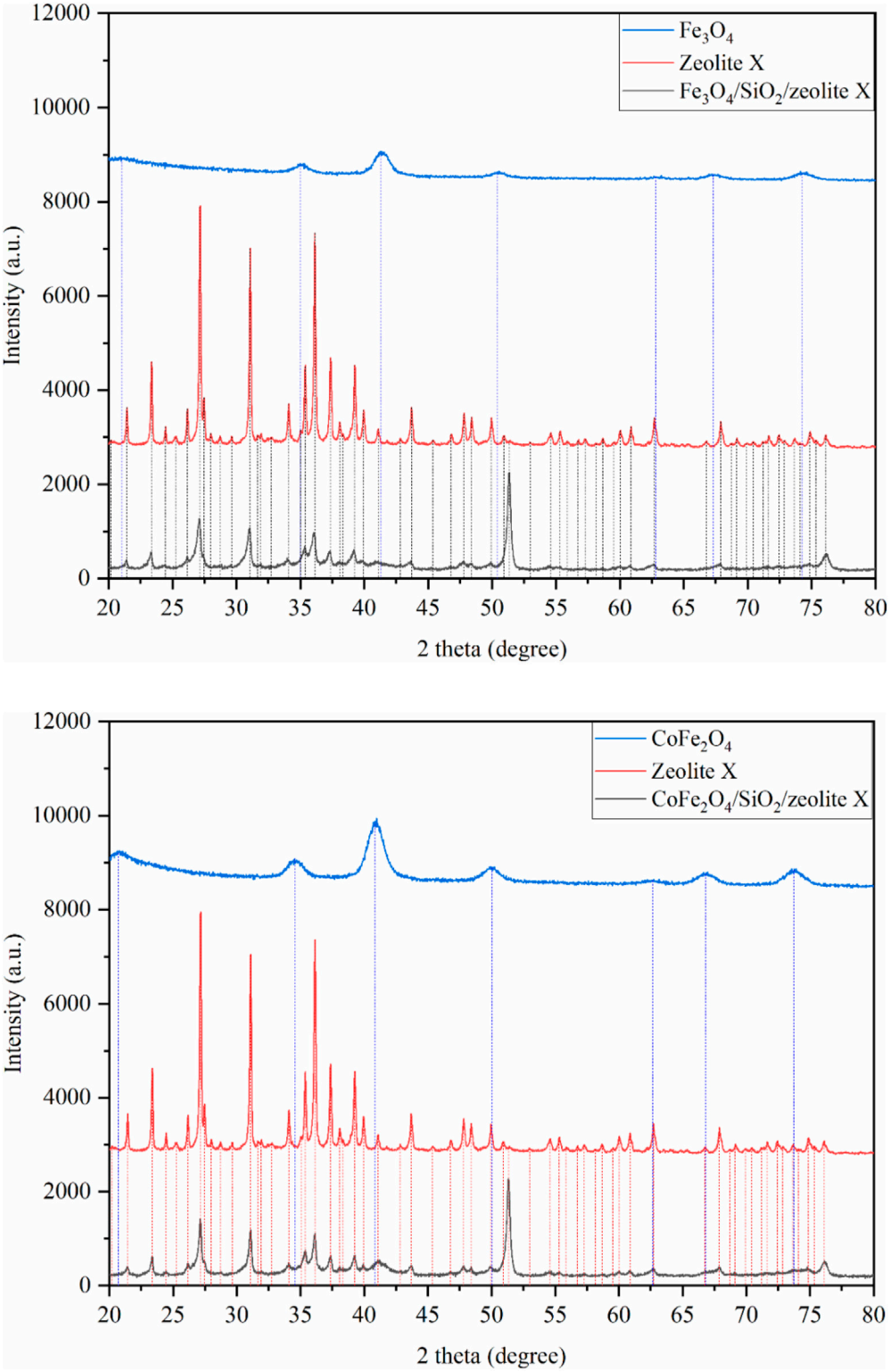

FIGURE 7
XRD patterns of Fe_3O_4/SiO_2/zeolite X (top) and $CoFe_2O_4/SiO_2$/zeolite X (bottom). The vertical lines are peak positions from individual fits.

by the vortex mixer for 1 h again. The mixture was heated in a rotation oven at 95°C for 4 days. For the Fe_3O_4/SiO_2/Na,K-CHA or the $CoFe_2O_4/SiO_2$/Na,K-CHA, the particles were mixed with 2 M NaCl solution, shaken at 140 rpm for 15 min, and then heated at 100°C for 15 min, followed by a single wash with DI water. The process was repeated six times, and the final product was washed with DI water three times and dried at 60°C. The synthesised M_xO_y/SiO_2/zeolite contained ca. 26%–29% of M_xO_y/SiO_2.

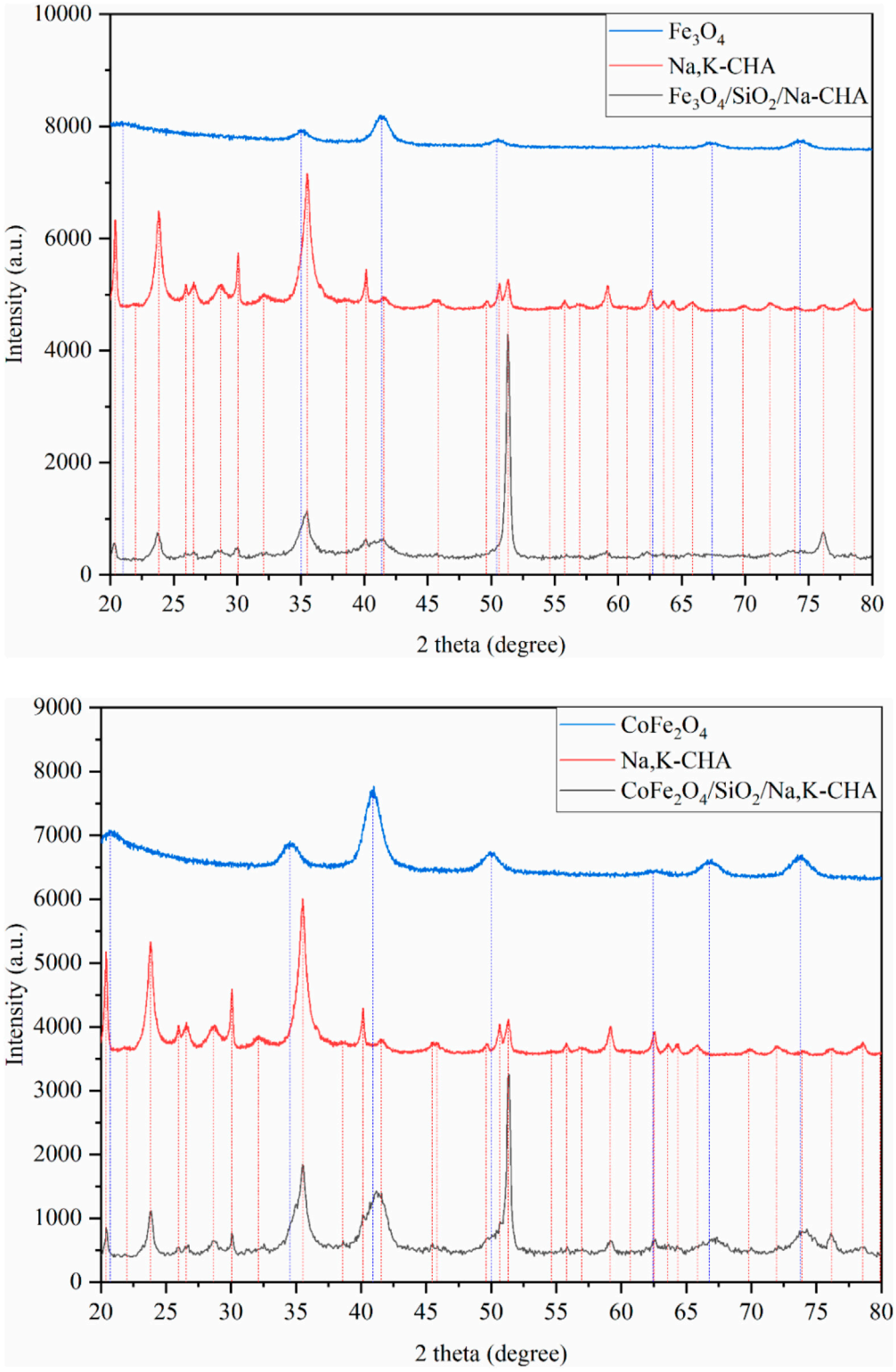

FIGURE 8
XRD patterns of Fe_3O_4/SiO_2/Na,K-CHA (top) and $CoFe_2O_4/SiO_2$/Na,K-CHA (bottom). The vertical lines are peak positions from individual fits.

All dried M_xO_y/SiO_2/zeolite particle samples were dispersed in DI water in a centrifuge tube and magnetically collected by trapping against the side of the tube using a neodymium magnet from the outside. The particles that were not attracted by the magnet were removed from the tube with the water. The process was repeated three times, and then the final selected samples were dried at 60°C. The recovered masses were in the range of 40%–56% of the initial masses.

TABLE 3 Data from peak fittings of the XRD data shown in Figures 6–8.

Sample	2 theta (°)	Intensity form baseline	Peak area	FWHM (°)
Zeolite A	31.62	5309	754	0.13
	38.01	1,179	187	0.15
Fe_3O_4/SiO_2/zeolite A	31.57	1,112	324	0.21
	37.96	250	63	0.23
$CoFe_2O_4/SiO_2$/zeolite A	31.59	3,017	568	0.16
	37.98	722	128	0.15
Zeolite X	31.10	4,076	743	0.15
	37.36	1,719	337	0.17
Fe_3O_4/SiO_2/zeolite X	31.05	798	324	0.32
	37.33	316	132	0.36
$CoFe_2O_4/SiO_2$/zeolite X	31.10	914	351	0.26
	37.36	352	108	0.26
Na.K-CHA	35.11	2,292	2,155	0.68
	59.17	411	202	0.39
Fe_3O_4/SiO_2/Na,K-CHA	35.52	764	772	0.83
	59.10	134	85	0.80
$CoFe_2O_4/SiO_2$/Na,K-CHA	35.52	1,312	1,401	0.89
	59.17	214	145	0.54

TABLE 4 Elemental compositions (oxygen not detected) of the bare zeolite A, Fe_3O_4/SiO_2/zeolite A, and $CoFe_2O_4/SiO_2$/zeolite A.

Target element	Zeolite A		Fe_3O_4/SiO_2/zeolite A		$CoFe_2O_4/SiO_2$/zeolite A		
	wt%	Molar ratio to Al	wt%	Molar ratio to Al	wt%	Molar ratio to Al	Molar ratio to Co
Na	12.9	0.5	3.9	0.5	7.3	0.6	
Al	33.1	1.0	8.8	1.0	13.8	1.0	
Si	51.3	1.5	11.6	1.3	15.9	1.1	
Fe			75.7	4.2	47.5	1.7	3.2
Co					15.5	0.5	1.0

TABLE 5 Elemental compositions (oxygen not detected) of the bare zeolite X, Fe_3O_4/SiO_2/zeolite X, and $CoFe_2O_4/SiO_2$/zeolite X.

Target element	Zeolite X		Fe_3O_4/SiO_2/zeolite X		$CoFe_2O_4/SiO_2$/zeolite X		
	wt%	Molar ratio to Al	wt%	Molar ratio to Al	wt%	Molar ratio to Al	Molar ratio to Co
Na	15.2	0.6	5.1	0.6	8.0	0.7	
Al	30.1	1.0	10.1	1.0	13.2	1.0	
Si	52.8	1.7	14.9	1.4	18.7	1.4	
Fe			69.9	3.3	38.5	1.4	1.9
Co					21.2	0.7	1.0

10.3389/fenvc.2024.1445482

TABLE 6 Elemental compositions (oxygen not detected) of the bare Na,K-CHA, Fe_3O_4/SiO_2/Na,K-CHA, and $CoFe_2O_4/SiO_2$/Na,K-CHA.

Target element	Na,K-CHA		Fe_3O_4/SiO_2/Na,K-CHA		$CoFe_2O_4/SiO_2$/Na,K-CHA		
	wt%	Molar ratio to Al	wt%	Molar ratio to Al	wt%	Molar ratio to Al	Molar ratio to Co
Na	8.2	0.5	2.4	0.7	2.2	0.7	
Al	20.7	1.0	4.1	1.0	4.0	1.0	
Si	68.6	3.2	11.6	2.7	12.0	2.9	
K	1.9	0.1	0.1	0.0	0.0	0.0	
Fe			81.8	9.6	62.9	7.6	3.5
Co					18.8	2.1	1.0

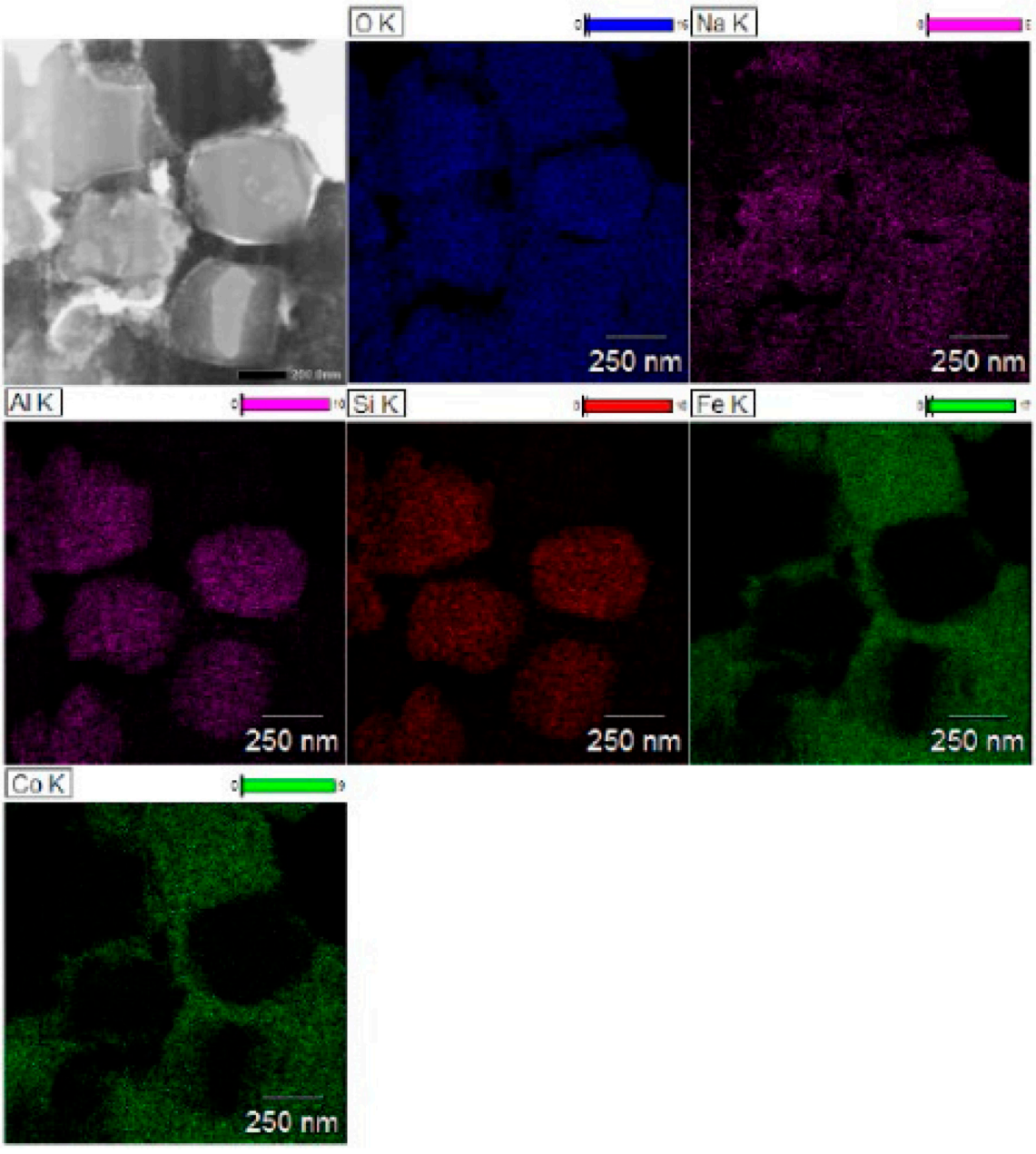

FIGURE 9
TEM images and EDS mapping of the sliced $CoFe_2O_4/SiO_2$/zeolite A.

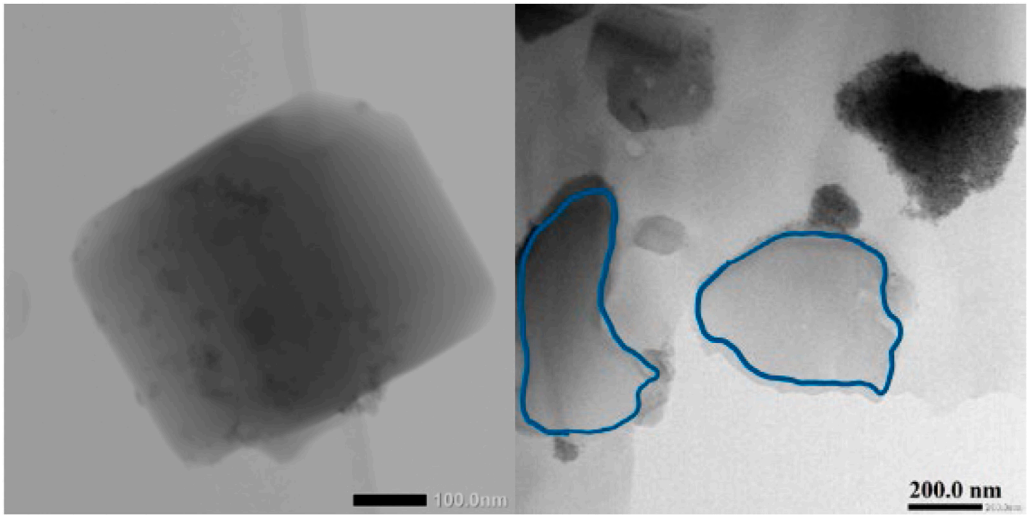

FIGURE 10
TEM images of Fe_3O_4/SiO2/zeolite A (left) and the sliced Fe_3O_4/SiO_2/zeolite A particles. The area enclosed by the blue contour is the cross section of a single particle sliced by the FIB.

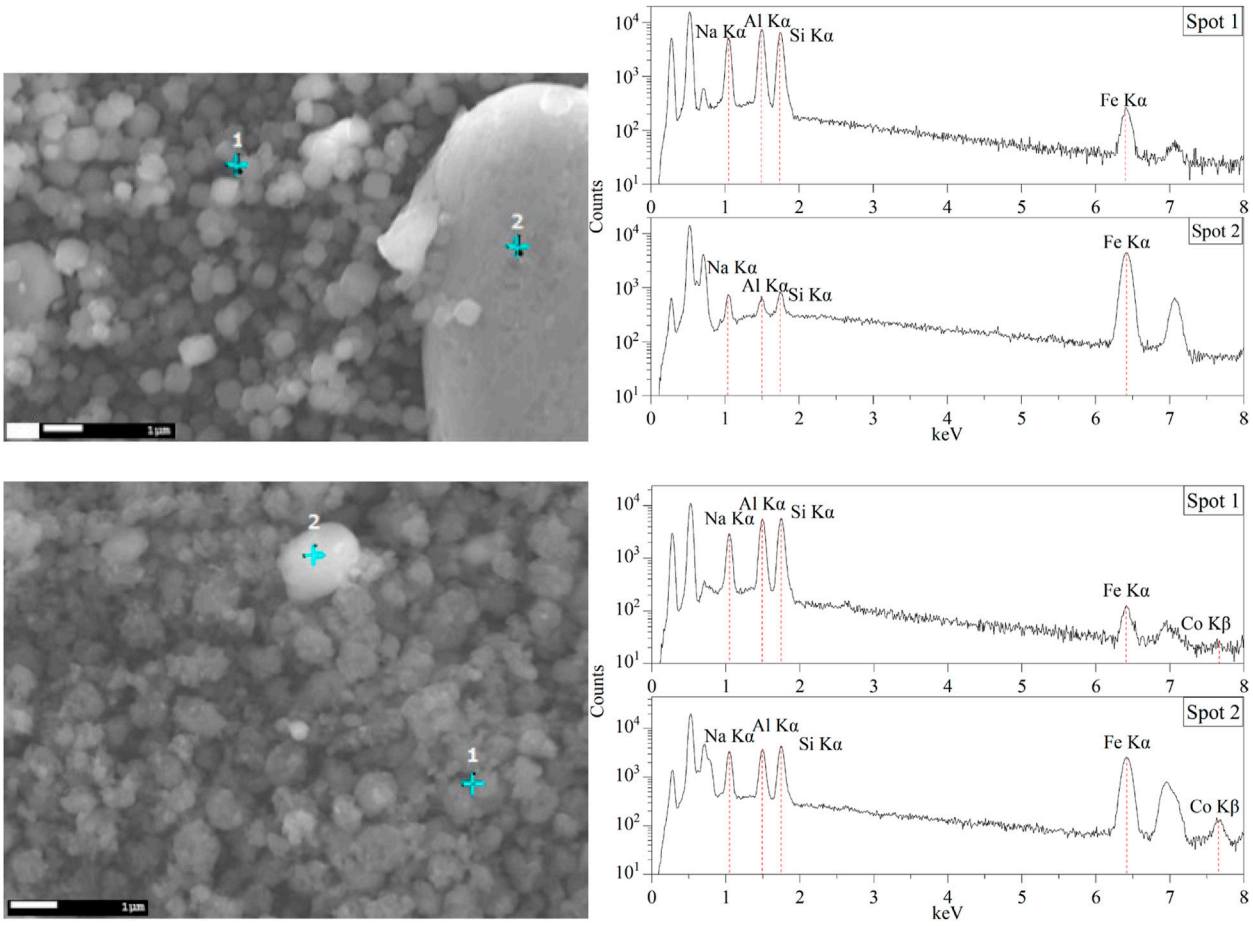

FIGURE 11
SEM images and energy-dispersive X-ray spectra of Fe_3O_4/SiO_2/zeolite A (top) and $CoFe_2O_4/SiO_2$/zeolite X (bottom).

10.3389/fenvc.2024.1445482

TABLE 7 Derived magnetic properties of M_xO_y/SiO_2/zeolite (H_c is the coercive field, M_s is the saturation magnetisation, and M_r is the remnant magnetisation).

Sample	H_c	M_s	M_r	M_r/M_s
Fe_3O_4/SiO_2/zeolite A	−0.032	9.476	0.110	0.012
	0.029	−9.477	0.147	0.016
$CoFe_2O_4/SiO_2$/zeolite A	−0.022	15.500	0.170	0.011
	0.023	−15.500	−0.178	0.011
Fe_3O_4/SiO_2/zeolite X	0.019	8.500	−0.060	−0.007
	0.022	−8.500	−0.060	0.007
$CoFe_2O_4/SiO_2$/zeolite X	−0.032	10.900	0.200	0.018
	0.057	−10.900	−0.333	0.031
Fe_3O_4/SiO_2/Na,K-CHA	−0.029	13.700	0.108	0.008
	−0.003	−13.700	0.014	−0.001
$CoFe_2O_4/SiO_2$/Na,K-CHA	−0.038	24.700	0.800	0.032
	0.029	−24.700	−0.400	0.016

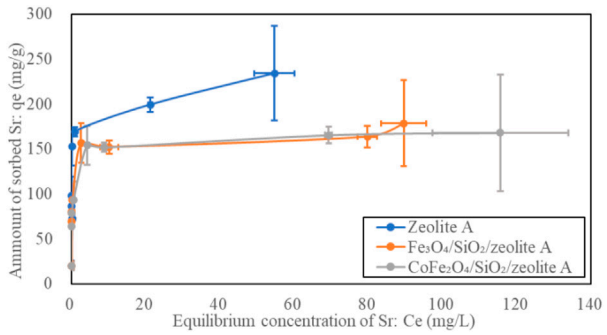

FIGURE 12
Sr adsorption isotherms of zeolite A, Fe_3O_4/SiO_2/zeolite A and $CoFe_2O_4/SiO_2$/zeolite A.

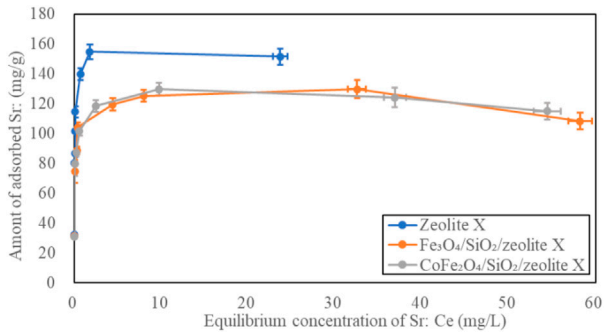

FIGURE 13
Sr adsorption isotherms of zeolite X, Fe_3O_4/SiO_2/zeolite X and $CoFe_2O_4/SiO_2$/zeolite X.

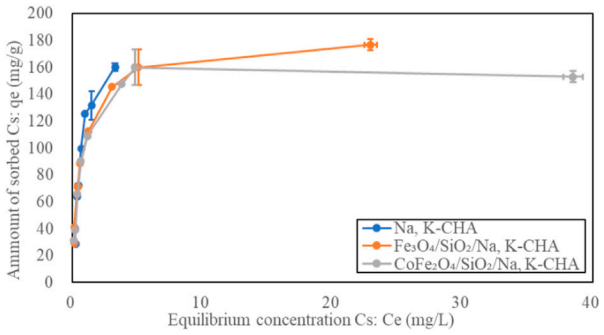

FIGURE 14
Cs adsorption isotherms of Na,K-CHA, Fe_3O_4/SiO_2/Na,K-CHA and $CoFe_2O_4/SiO_2$/Na,K-CHA.

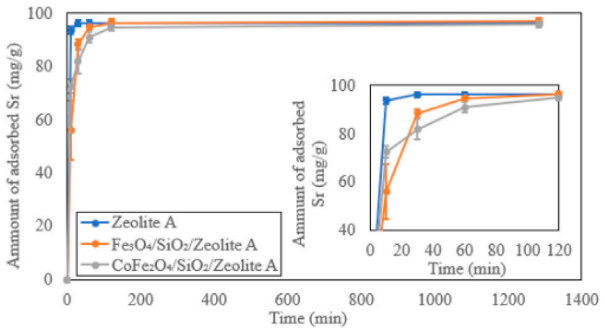

FIGURE 15
Time-dependent Sr adsorption on zeolite A, Fe_3O_4/SiO_2/zeolite A and $CoFe_2O_4/SiO_2$/zeolite A.

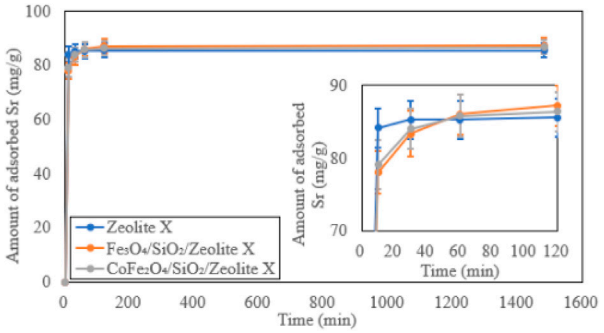

FIGURE 16
Time-dependent Sr adsorption on zeolite X, Fe_3O_4/SiO_2/zeolite X and $CoFe_2O_4/SiO_2$/zeolite X.

2.5 Sr^{2+} or Cs^+ adsorption experiments

2.5.1 Sr or Cs adsorption isotherms

A 10 mg portion of M_xO_y/SiO_2/zeolite A, M_xO_y/SiO_2/zeolite X, M_xO_y/SiO_2/Na,K-CHA, or the bare zeolite sample was dispersed in a 50 mL centrifuge tube with 10 mL of Sr solution in the range of 20 to

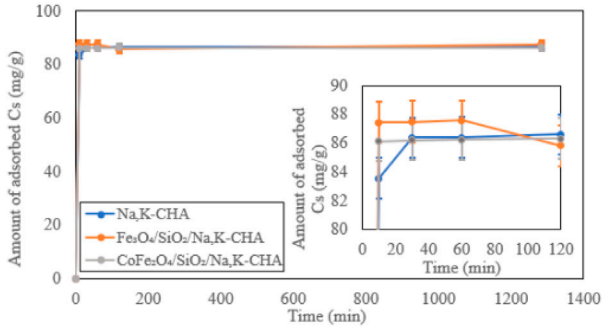

FIGURE 17
Time-dependent Cs adsorption on Na,K-CHA, Fe_3O_4/SiO_2/Na,K-CHA and $CoFe_2O_4/SiO_2$/Na,K-CHA.

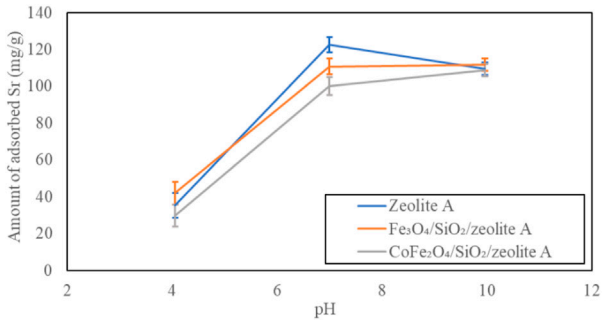

FIGURE 18
pH dependent Sr adsorption on zeolite A, Fe_3O_4/SiO_2/zeolite A and $CoFe_2O_4/SiO_2$/zeolite A.

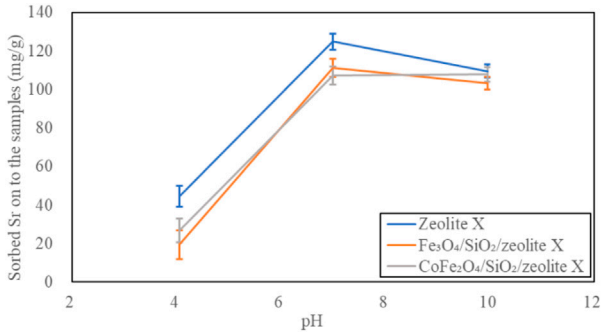

FIGURE 19
pH dependent Sr adsorption on zeolite X, Fe_3O_4/SiO_2/zeolite X and $CoFe_2O_4/SiO_2$/zeolite X.

278 mg/L for the M_xO_y/SiO_2/zeolite A and the bare zeolite A or 33 to 176 mg/L for the M_xO_y/SiO_2/zeolite X and the bare zeolite X, or Cs solution in the range of 18 to 202 mg/L for the M_xO_y/SiO_2/Na,K-CHA or 30 to 161 mg/L for the bare Na,K-CHA. The Sr or Cs solutions were prepared from $Sr(NO_3)_2$ or $CsNO_3$ and ultrapure water. No pH adjustments were made. The tubes were shaken at 140 rpm for 24 h at ambient temperature. The exchanged solutions

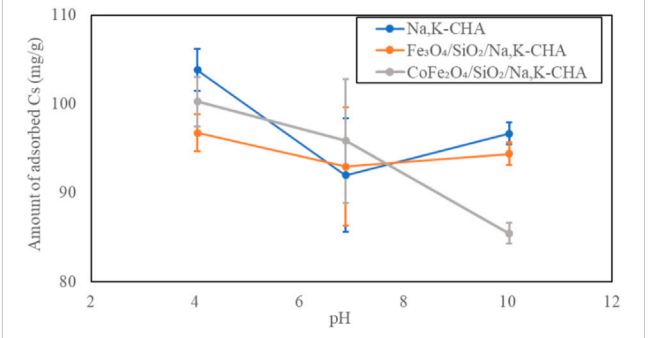

FIGURE 20
pH dependent Cs adsorption on Na,K-CHA, Fe_3O_4/SiO_2/Na,K-CHA and $CoFe_2O_4/SiO_2$/Na,K-CHA.

were filtered through 0.22 µm filters and then a small amount of each exchanged solution was diluted by ultrapure 2% HNO_3 to give a total volume of 10 mL with a Sr or Cs level below 0.5 mg/L; these were then used for ICP-MS measurements.

2.5.2 Time-dependent Sr or Cs adsorption capacities

A 10 mg of portion of M_xO_y/SiO_2/zeolite A, M_xO_y/SiO_2/zeolite X, M_xO_y/SiO_2/Na,K-CHA, or the bare zeolite A, zeolite X, or Na,K-CHA was dispersed in a 50 mL centrifuge tube with 30 mL of the Sr solution (97 mg/L for M_xO_y/SiO_2/zeolite A and the bare zeolite A or 88 mg/L for M_xO_y/SiO_2/zeolite X and the bare zeolite X) or the Cs solution (89 mg/L for M_xO_y/SiO_2/Na,K-CHA and the bare Na,K-CHA). The initial pH values of Sr solutions were 7.42 for M_xO_y/SiO_2/zeolite A and the bare zeolite A and 6.48 for M_xO_y/SiO_2/zeolite X and the bare zeolite X. The initial pH value of Cs solution was 7.33. The samples were exchanged by a vortex mixier at 900 rpm, and aliquots of the exchanged solution were taken out at 10, 30, 60, 120, and 1,440 min. They were filtered and prepared for the ICP-MS measurements in the same way as described for the Sr or Cs adsorption isotherm experiments.

2.5.3 pH-dependent Sr or Cs adsorption capacities

The experimental method was almost the same as the Sr or Cs adsorption isotherms; however, the pH values of the Sr or Cs solutions were buffered by the use of either HEPES (4-(2-hydroxyethyl)-1-piperazineethanesulfonic acid) or CAPS (N-cyclohexyl-3-aminopropanesulfonic acid). Before making the Sr or Cs solutions, a pH 4 solution was made from 50 mM HEPES and 1 M HCl, and pH 7 and 10 solutions were made from 50 CAPS and 1 M to 0.1 M NaOH, as required. Then, the $Sr(NO_3)_2$ or $CsNO_3$ was added to the pH adjusted solutions (Table 1).

2.6 Characterisation

The M_xO_y/SiO_2/zeolite A, M_xO_y/SiO_2/zeolite X, and M_xO_y/SiO_2/Na,K-CHA products were analysed by powder x-ray diffraction (Bruker D2, Co-anode, K_α = 1.79026 Å), and a Bruker D8 Advance (Cu-anode, K_α = 1.5406 Å) was used for the Cs

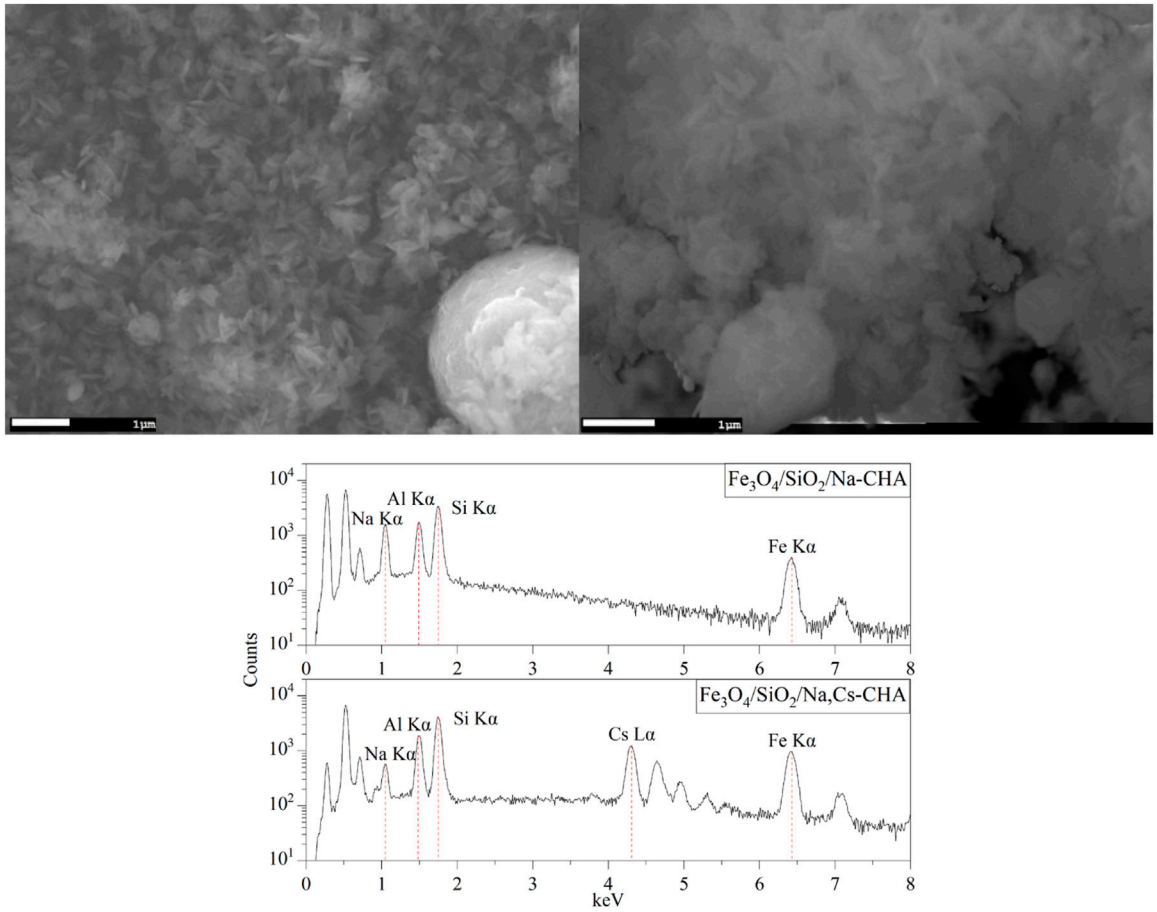

FIGURE 21
SEM images of Fe_3O_4/SiO_2/Na-CHA (right) and Fe_3O_4/SiO_2/Cs,Na-CHA (left).

exchanged M_xO_y/SiO_2/Na,K-CHA analysis. The elemental compositions of the products were analysed by XRF (Bruker S8 Tiger, Rh target) as pressed pellets using a wax binder (SpectroBlend® 44 μm Powder, Chemplex). The ratio of the bare zeolite to wax was 1:4 to 1:1.6, and the ratio of M_xO_y/SiO_2/zeolite A, M_xO_y/SiO_2/zeolite X, and M_xO_y/SiO_2/Na,K-CHA samples to wax was about 1:2.3 to 1:5.9. The Raman spectra of M_xO_y samples were obtained by a Renishaw inVia Raman microscope with a 532 nm green laser excitation (Cobalt Samba 100) with 0.5 mW power for Fe_3O_4 and 1.0 mW power for $CoFe_2O_4$. The magnetic properties of the Fe_3O_4 sample were measured by magnetic property measurement system (Quantum Design MPMS XL-5) at 27°C, and the other samples were measured by vibrating sample magnetometry (VSM, Quantum Design MPMS 3) at 27°C.

Electron microscopy was performed by SEM-EDS (JSM-7800F, JEOL), and the sample morphology and size distribution were observed by TEM-EDS (Thermo Fisher Scientific FEI Ralos F200 or JEOL JEM-2800). For cross section measurements, particles of M_xO_y/SiO_2/zeolite A, M_xO_y/SiO_2/zeolite X, and M_xO_y/SiO_2/Na,K-CHA were sliced by Focused Ion Beam System (JEOL JIB-40).

The Sr^{2+} or Cs^+ concentrations in the adsorption experiments were measured by ICP-MS (Perkin Elmer NexION™ 300). The $RbNO_3$ or $Y(NO_3)_3$ was used as an internal standard for the measurements.

3 Results and Discussion

3.1 Characterisation of M_xO_y and M_xO_y/SiO_2 materials

3.1.1 Structure analysis

The XRD patterns of the pure and silica coated Fe_3O_4 and $CoFe_2O_4$ nanoparticles were obtained to confirm their identity and purity (Figure 1). The pattern for Fe_3O_4 is indexed based on the ICDD PDF file 04-007-1,060 and that for $CoFe_2O_4$ from file 00-003-0864. The XRD peaks of both Fe_3O_4/SiO_2 and $CoFe_2O_4/SiO_2$ were shifted slightly from their pure particles and this may be due to covalent bonds between the metal oxide nanoparticle surfaces and the SiO_2 layers, the covalent bonds may form while the SiO_2 coating is forming by reacting with -OH groups on the Fe_3O_4 and $CoFe_2O_4$ surfaces (Babu et al., 2013).

For the iron oxide sample, the XRD patterns of Fe_3O_4 and γ-Fe_2O_3 are essentially identical. To confirm the correct spinel has formed, Raman spectra were also obtained (Figure 2). The iron sample had a Raman peak at 683 cm^{-1} that is in good agreement with the reported A_{1g} phonon mode of Fe_3O_4 (Pazik et al., 2013). The $CoFe_2O_4$ sample had Raman peaks at 301, 467 and 680 cm^{-1} that can be assigned to the E_g. T_{1g}, and A_{1g} phonon modes, respectively (Chandramohan et al., 2011).

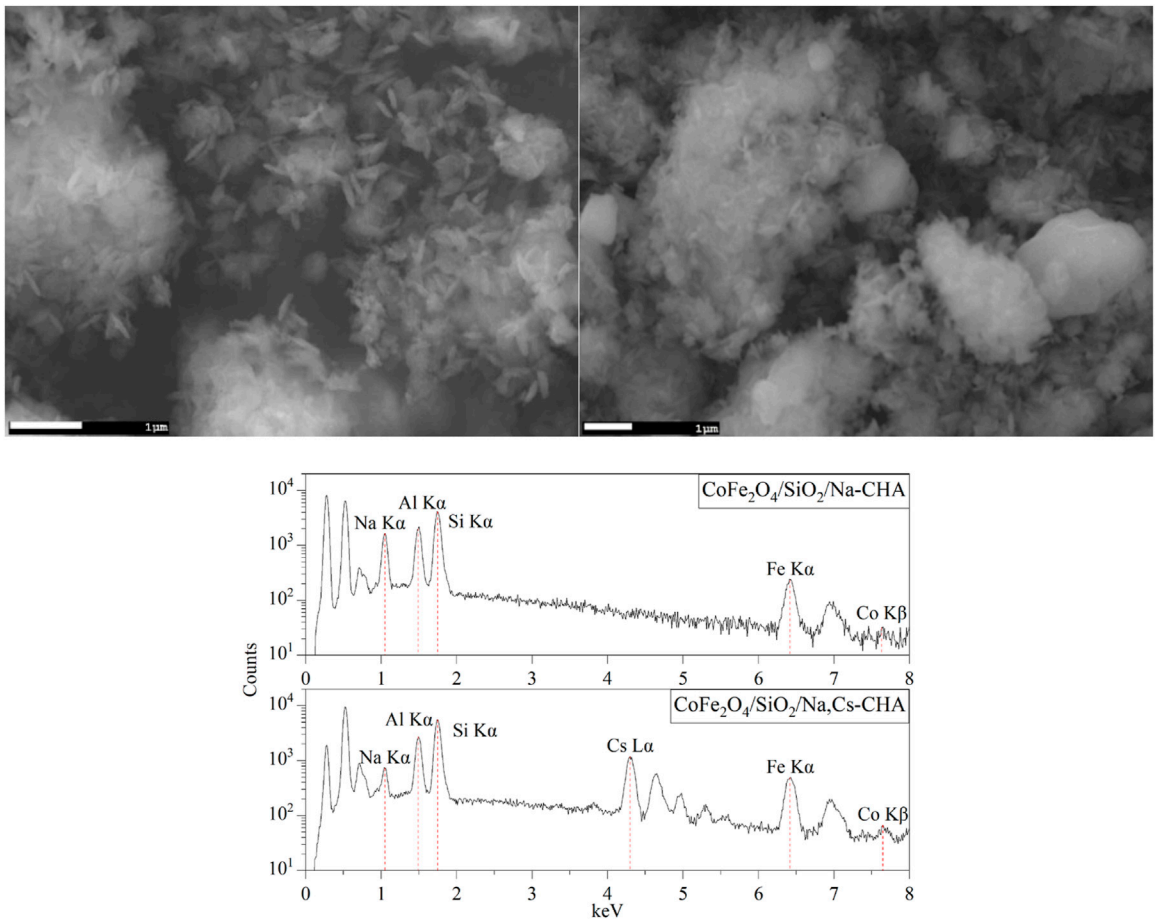

FIGURE 22
SEM images of $CoFe_2O_4/SiO_2$/Na-CHA (right) and $CoFe_2O_4/SiO_2$/Cs,Na-CHA (left).

TEM was used to measure the Fe_3O_4 and $CoFe_2O_4$ particle sizes, and the SiO_2 thickness on $CoFe_2O_4$ was also obtained (Figures 3, 4). It was observed that the $CoFe_2O_4/SiO_2$ sample had uniform ca. 2 nm SiO_2 coatings on the 7.5 (±1.5) nm $CoFe_2O_4$ particles. However, in the TEM image of Fe_3O_4/SiO_2, a uniform thickness SiO_2 coating was not observed even though the amount of TEOS (the silica source) was higher than for the $CoFe_2O_4/SiO_2$ synthesis. There are regions that appear to show an amorphous layer on the outside of particles and Si is detected by TEM-EDS so we interpret this as a less uniform and thinner (less than 2 nm) coating formed on the 8.0 (±1.8) nm Fe_3O_4 particles (the TEM used cannot detect less than about a 1 nm thickness of a low density SiO_2 layer). The difference of SiO_2 thickness might be caused by the synthesis temperature, it varied between about 20°C and 30°C during the ultrasonification process, and it might effect the solubility and viscosity of the synthesis medium (Tan et al., 1987).

3.1.2 Magnetic property

The magnetisation loops of both the bare and silica-coated Fe_3O_4 and $CoFe_2O_4$ nanoparticles at 300 K are shown in Figure 5. The saturation magnetisation of Fe_3O_4 (58.9 emu/g) was 10.7 emu/g lower than that of $CoFe_2O_4$ (69.6 emu/g) (Table 2). For both materials the values are in the expected range: 5.5 nm particles of Fe_3O_4 had a reported value of 50 emu/g at 12 kOe (Li et al., 2010), 8 nm particles 47 emu/g at 60 kOe (Lemine et al., 2012), and 5.9 to 8.9 nm particles of $CoFe_2O_4$ had 50.2 to 58.7 emu/g at 10 kOe (Yáñez-Vilar et al., 2009). The Fe_3O_4 and $CoFe_2O_4$ particles synthesised here have similar or slightly higher saturation magnetisations than previously reported.

The saturation magnetisation of $CoFe_2O_4$ can be changed by the ratio of Co and Fe. $CoFe_2O_4$ has an inverse-spinel structure that the general formula is B (AB)O_4 (A is a divalent ion and B is a trivalent ion), half of the B ions occupy octahedral sites while other half occupy tetrahedral sites (Smart and Moore, 2012). The average mole ratio of Co and Fe was 1.0 to 2.7. In such a structure, the occupancy of Fe^{2+} ions in the octahedral sites increased by increasing the concentration of Fe, and the Co^{2+} and Fe^{3+} ions occupy the tetrahedral sites, as a result, the saturation magnetisation of $CoFe_2O_4$ was higher than Fe_3O_4 by having a strong surface anisotropy (Biswal et al., 2013).

After SiO_2 coating of the Fe_3O_4 and $CoFe_2O_4$ particles, the saturation magnetisations in units of emu/g dropped. This has been previously seen and studied for $NiFe_2O_4$ and attributed to both the mass having a substantial nonmagnetic SiO_2 component but more significantly the silica coating increasing the metal spin canting at the interface causing larger magnetic anisotropy of the core particle surface spins (Umut et al., 2021). The decreasing of saturation magnetisation of $CoFe_2O_4/SiO_2$ (57.6 emu/g) was less than that

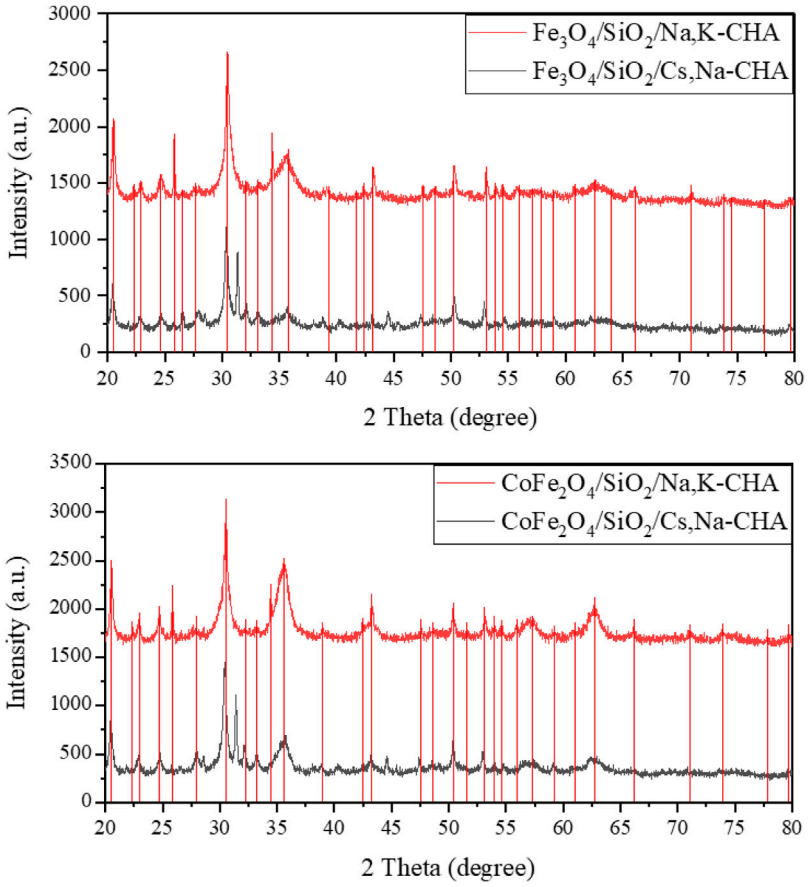

FIGURE 23
Powder XRD patterns of materials before and after the Cs adsorption experiments of Fe_3O_4/SiO_2/Na,K-CHA (top) and $CoFe_2O_4/SiO_2$/Na,K-CHA (bottom). The vertical lines are peak positions from individual fits.

of $F_{e3}O_4/SiO_2$ (34.0 emu/g). This could be due to the relative distributions of Co^{2+}, Fe^{2+} and Fe^{3+} ions in the tetrahedral sites of the $CoFe_2O_4/SiO_2$, or aggregation of the $CoFe_2O_4$ particles might have occurred through the SiO_2 coating process.

3.2 Characterisation of M_xO_y/SiO_2/ zeolite materials

3.2.1 Structure analysis

The XRD patterns of the pure M_xO_y, pure zeolite, and composite M_xO_y/SiO_2/zeolite materials are shown in Figures 6–8. These confirm in all cases the target zeolite has formed in good purity with the coated particles, peaks for the zeolite match those for zeolite A in the ICSD PDF file 00-039-0222, zeolite X in file 00-038-0237 and zeolite chabazite in file 00-019-1178. All M_xO_y/SiO_2/ zeolite products have broad peaks at ca. 41°, consistent with the presence of a spinel ferrite phase. There is no evidence of crystalline SiO_2, which is in keeping with a thin amorphous coating on the spinel oxide particles. All excluding $CoFe_2O_4/SiO_2$/zeolite A also have a sharp peak at around 51°, this is likely due to the background holder as the specimens had to be prepared as thin layers held in place with vaseline. To confirm whether zeolite frameworks of the M_xO_y/SiO_2/zeolite had the same crystallinity as the pure zeolite, two XRD peaks for each of the M_xO_y/SiO_2/zeolite and the pure zeolite at the same positions were fitted (Table 3). The FWHM values, excluding $CoFe_2O_4/SiO_2$/zeolite A, were at least 0.08° larger than that of the pure zeolite equivalent. The peak broadening is indicative of reduced crystallinity and could be due to either the formation of smaller zeolite particles or the presence of framework defects.

From the bulk elemental compositions as derived from XRF measurements, Tables 4–6, all Si/Al ratios of M_xO_y/SiO_2/zeolites were close to theoretical Si/Al ratios of zeolite A (1.0), zeolite X (1.2) and CHA (2.3) (Robson, 2001). Although the silica coating of the ferrite particles will increase the Si/Al ratios, the change will be insignificant given the majority of the Si and Al present are in the zeolite particles and will be much less than the errors associated with the measurements. The Na/Al and K/Al ratios were lower than expected but consistent within the expected error limits (ca. relative 10%) for each zeolite type. There may be some Na^+ adsorbed onto the SiO_2 layers as SiO^--Na^+ (Andriyko et al., 2015), because the TEM-EDS maps for Na shows there was some signal on the $CoFe_2O_4/SiO_2$ nanoparticles (Figure 9) as well as zeolite particles.

The TEM images of Fe_3O_4/SiO_2/zeolite A and its cross-section (Figure 10) show the Fe_3O_4/SiO_2 nanoparticles are attached to zeolite surfaces, furthermore the TEM-EDS of $CoFe_2O_4/SiO_2$/ zeolite A shows most of the $CoFe_2O_4/SiO_2$ nanoparticles are aggregated on the outside of the zeolite A. The aggregated

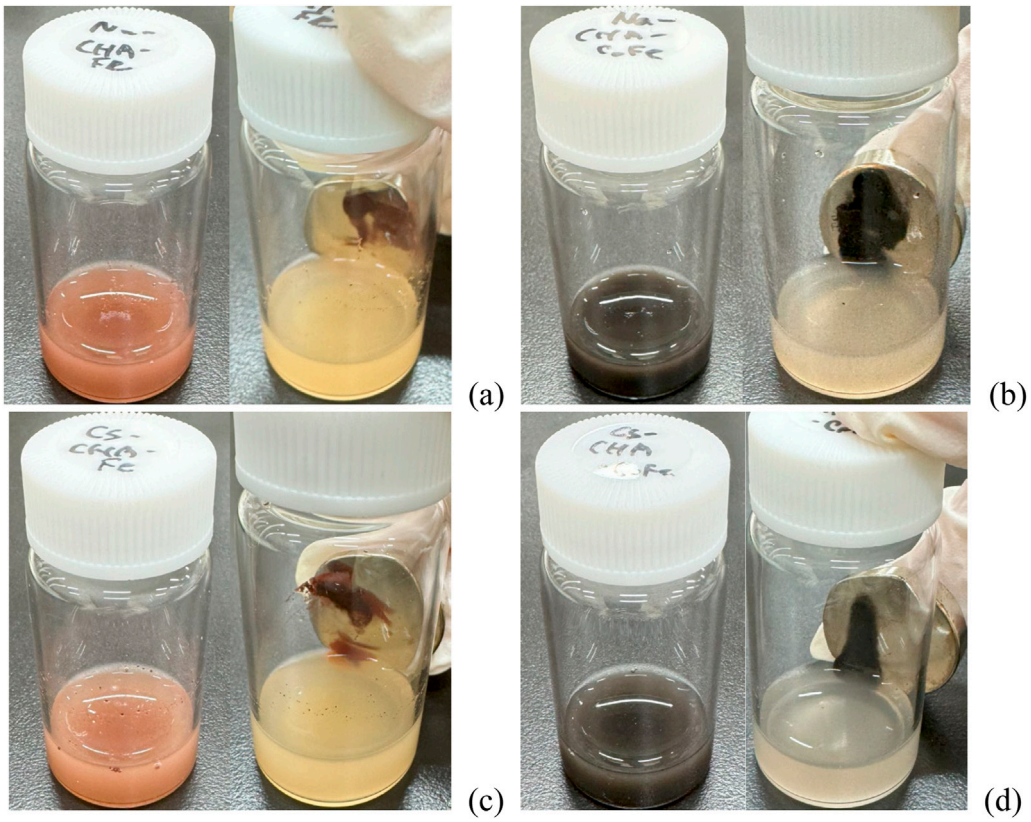

FIGURE 24
Before and after magnetic separations of **(A)** Fe_3O_4/SiO_2/Na,K-CHA, **(B)** $CoFe_2O_3/SiO_2$/Na,K-CHA, **(C)** Fe_3O_4/SiO_2/Cs,Na-CHA and **(D)** $CoFe_2O_3/SiO_2$/Cs,Na-CHA by a neodymium magnet (7.5 kgf).

particles formed as single big particles (Figure 9). It could be assumed that the silicon source for the formation of the zeolite might be also used to connect the M_xO_y/SiO_2 particles. Therefore, it could be assumed the Fe_3O_4/SiO_2 and $CoFe_2O_4/SiO_2$ nanoparticles are unlikely to be detached from the zeolite surfaces during the cation-exchange processes. From the SEM-EDS of Fe_3O_4/SiO_2/zeolite A and $CoFe_2O_4/SiO_2$/zeolite X, the Si signal was slightly higher than the Al on the spot of the aggregated Fe_3O_4/SiO_2 and $CoFe_2O_4/SiO_2$ (Figure 11).

3.2.2 Magnetic properties

Magnetic properties for all samples are listed in Table 7. The maximum magnetisations of the Fe_3O_4/SiO_2/zeolite and $CoFe_2O_4/SiO_2$/zeolite were 8.5 emu/g and 10.9 emu/g, respectively, these are higher than the Fe_3O_4/Na,K-CHA and $CoFe_2O_4$/Na,K-CHA materials that were previously reported at 5.3 emu/g and 6.3 emu/g, respectively (Ito et al., 2023). The maximum magnetisations of the M_xO_y/SiO_2/zeolite tended to increase when the ratio of M_xO_y/SiO_2 and M_xO_y/SiO_2/zeolite was higher, excluding the $CoFe_2O_4/SiO_2$/zeolite X. This tendency agrees with the work of Faghihian et al. (Faghihian et al., 2014). For the $CoFe_2O_4/SiO_2$/zeolite X, it could be assumed there might be smaller aggregated $CoFe_2O_4/SiO_2$ particles such as seen in Figure 11. The M_r/M_s values were all less than 0.1 kOe, Table 7 and Supplementary Figures S1–S3, this means the M_xO_y/SiO_2 particles in the zeolite materials were still superparamagnetic. It could be supposed the SiO_2 thin layer on the M_xO_y particles protect them as single domains.

3.3 Sr^{2+} and Cs^+ adsorption properties

The Sr^{2+} adsorption isotherms of the bare zeolite A, Fe_3O_4/SiO_2/zeolite A and $CoFe_2O_4/SiO_2$/zeolite A are shown in Figure 12. The shapes of the isotherm curves for Fe_3O_4/SiO_2/zeolite A and $CoFe_2O_4/SiO_2$/zeolite A are almost the same. The maximum q_e of bare zeolite A was over 56 mg/g higher than the Fe_3O_4/SiO_2/zeolite A and $CoFe_2O_4/SiO_2$/zeolite A. The Fe_3O_4/SiO_2/zeolite X and $CoFe_2O_4/SiO_2$/zeolite X had also the similar isotherm curves as the Fe_3O_4/SiO_2/zeolite A and $CoFe_2O_4/SiO_2$/zeolite A (Figure 13). The maximum q_e of bare zeolite X was over 25 mg/g higher than them. The Cs^+ adsorption isotherms of the bare Na,K-CHA, Fe_3O_4/SiO_2/Na,K-CHA and $CoFe_2O_4/SiO_2$/Na,K-CHA are shown in Figure 14. The q_e of both Fe_3O_4/SiO_2/Na,K-CHA and $CoFe_2O_4/SiO_2$/Na,K-CHA were about 15 mg/g different from the bare Na,K-CHA at 3 mg/L. The lower q_e values for the composites are expected as the weight fraction of zeolite within them are on the order of 20%–40% from the XRF data.

The Time-dependent Sr^{2+} adsorption behaviours on the bare zeolite A, Fe_3O_4/SiO_2/zeolite A and $CoFe_2O_4/SiO_2$/zeolite A are shown in Figure 15. Most Sr^{2+} was exchanged in the first 30 min by the bare zeolite A. Equilibrium is reached about 90 min faster than both Fe_3O_4/SiO_2/zeolite A and $CoFe_2O_4/SiO_2$/zeolite A. The bare zeolite X also adsorbed most Sr^{2+} within 30 min, and the adsorption speeds of both Fe_3O_4/SiO_2/zeolite X and $CoFe_2O_4/SiO_2$/zeolite X were also 30 to 90 min slower than the bare zeolite X (Figure 16).

This could be due to restricted access of the solution to the surface of the zeolite particles in the composites. At the end of the Sr adsorption experiments, similar trends of slight pH increases of the solutions were observed in Fe_3O_4/SiO_2/zeolite A, $CoFe_2O_4/SiO_2$/zeolite A and the bare zeolite A with final values of 8.40 ± 0.11, 8.17 ± 0.08 and 9.43 ± 0.06 respectively, and for Fe_3O_4/SiO_2/zeolite X, $CoFe_2O_4/SiO_2$/zeolite X and the bare zeolite X with values of 7.67 ± 0.35, 7.00 ± 0.13 and 9.81 ± 0.01 respectively.

Both Fe_3O_4/SiO_2/Na,K-CHA and $CoFe_2O_4/SiO_2$/Na,K-CHA exchanged most Cs^+ within 10 min. The adsorption speeds were 20 min faster than the bare Na,K-CHA (Figure 17), however, the differences of the amount of adsorbed Cs^+ difference was about 3 to 4 mg/g, and it might be negligible. The final pH values of the solutions for Fe_3O_4/SiO_2/Na,K-CHA and $CoFe_2O_4/SiO_2$/Na,K-CHA were 7.58 ± 0.16 and 7.09 ± 0.16 respectively and similar to both M_xO_y/SiO_2/zeolite A and M_xO_y/SiO_2/zeolite X. The solution from the bare Na,K-CHA exhibited a pH of 6.71 ± 0.01 at the end of the Cs adsorption experiments.

The pH dependent Sr^{2+} adsorption on the bare zeolite A, Fe_3O_4/SiO_2/zeolite A and $CoFe_2O_4/SiO_2$/zeolite A are shown in Figure 18. All of them had the highest Sr^{2+} adsorption capacities at pH 7 to pH 10, and they were over 95 mg/g. The smallest capacities were at pH 4, and the amounts of adsorbed Sr^{2+} were almost half of the highest capacities, this is likely due to blocking of binding sites and reduction of local charges in the 6-ring windows due to protonation which impede Sr^{2+} binding. The bare zeolite X, Fe_3O_4/SiO_2/zeolite X and $CoFe_2O_4/SiO_2$/zeolite X had very similar Sr^{2+} adsorption characteristics to their zeolite A counterparts depending on pH (Figure 19).

The pH dependent Cs^+ adsorption on the bare Na,K-CHA, Fe_3O_4/SiO_2/Na,K-CHA and $CoFe_2O_4/SiO_2$/Na,K-CHA are shown in Figure 20. They had the highest Cs^+ capacities at pH 4, and it was over 94 mg/g. The Cs^+ capacity of $CoFe_2O_4/SiO_2$/Na,K-CHA decreased slightly until about 85 mg/g, as the pH increased. However, Both Na,K-CHA and Fe_3O_4/SiO_2/Na,K-CHA had the smallest Cs^+ capacities at pH 7. There is much less effect with pH than is seen for Sr^{2+} on zeolites A and X. This is not surprising as the CHA framework has a much higher Si/Al ratio leading to a lower surface charge so will be less likely to strongly bind protons, additionally the large Cs^+ cations site within cages at a greater distance from the framework than Sr^{2+}. This pH dependent behaviour of both Fe_3O_4/SiO_2/Na,K-CHA and $CoFe_2O_4/SiO_2$/Na,K-CHA are similar to the Fe_3O_4/Na,K-CHA and $CoFe_2O_4$/Na,K-CHA, which Fe_3O_4 and $CoFe_2O_4$ nanoparticles were incorporated at the edge of the zeolite particles (Ito et al., 2023).

The SEM images of before and after Cs adsorbed M_xO_y/SiO_2/Na,K-CHA are show in Figures 21, 22. The CHA particle structures did not change. From the SEM-EDS results, the Fe_3O_4/SiO_2 and $CoFe_2O_4/SiO_2$ particles seemed to not detach from the Na,K-CHA particles.

The XRD patterns before and after the Cs adsorption experiments of Fe_3O_4/SiO_2/Na,K-CHA and $CoFe_2O_4/SiO_2$/Na,K-CHA are shown in Figure 23. In both cases the patterns are nearly identical and indicate no significant degradation of the framework.

Dispersion and magnetic separation tests were performed for the M_xO_y/SiO_2/Na,K-CHA and M_xO_y/SiO_2/Cs,Na-CHA in deionised water (Figure 24). The particles started settling within 10 s when agitations were stopped, and most of the particles were attracted to a neodymium magnet (7.5 kgf) placed on the outside the vials. Some of the particles were weakly attracted to the magnet, therefore it was difficult to collect all particles by the magnet, and the water colours of both M_xO_y/SiO_2/Na,K-CHA and M_xO_y/SiO_2/Cs,Na-CHA were not clear after the process. However, the $CoFe_2O_3/SiO_2$/Na,K-CHA and $CoFe_2O_3/SiO_2$/Cs,Na-CHA particles were more strongly attracted by the magnet than the Fe_3O_4/SiO_2/Na,K-CHA and Fe_3O_4/SiO_2/Cs,Na-CHA particles because of their better magnetic characteristics (See Table 7).

4 Conclusions

SiO_2 coated Fe_3O_4 or $CoFe_2O_4$ nanoparticles incorporate and become attached to zeolite A, zeolite X, or Na,K-CHA when added to the synthesis mixture. The composites exhibit high magnetisation and superparamagnetic characteristics, even though they had some micro-sized aggregated Fe_3O_4/SiO_2 and $CoFe_2O_4/SiO_2$ particles. Most of the Fe_3O_4/SiO_2 or $CoFe_2O_4/SiO_2$ nanoparticles were attached on the zeolite surfaces, but they do not block access and the zeolites retain good Cs^+ or Sr^{2+} adsorption capacities. Furthermore, the time dependent Cs^+ or Sr^{2+} adsorptions of all M_xO_y/SiO_2/zeolites were almost as quick as the bare zeolite. Furthermore, it was confirmed the Fe_3O_4/SiO_2/Na-CHA and $CoFe_2O_4/SiO_2$/Na-CHA particles were not damaged after the Cs^+ adsorption experiments. Although no competitive ion exchange experiments were done in this work (e.g., Cs exchange in the presence of K), as there is no significant differences in the ion exchange behaviour of the magnetised systems compared to the pure zeolites we expect any reported behaviour of the pure systems would still be observed.

Data availability statement

The raw data supporting the conclusions of this article will be made available by the authors, without undue reservation.

Author contributions

AI: Data curation, Formal Analysis, Investigation, Methodology, Validation, Visualization, Writing–original draft, Writing–review and editing. GT: Investigation, Writing–review and editing. JH: Conceptualization, Funding acquisition, Methodology, Project administration, Resources, Supervision, Validation, Writing–original draft, Writing–review and editing.

Funding

The author(s) declare that financial support was received for the research, authorship, and/or publication of this article. JAH was part funded by EPSRC grant EP/S01019X/1, TRANSCEND: Transformative Science and Engineering for Nuclear Decommissioning.

Acknowledgments

The authors wish to acknowledge Futoshi Kanno of Environmental Evaluation Research Group, JAEA, for technical assistance with the TEM-EDS measurements of the Ion Slicer

and FIB processed MZ sample cross sections, Dr. Norman Day and Dr. Christopher Stark of the University of Birmingham for assistance with the ICP-MS measurements, and Dr. Mingee Chung and Jake Head of the University of Birmingham for assistance with the MPMS and VSM measurements. The authors are grateful to the Centre for Electron Microscopy, University of Birmingham for facilitating the use of TEM/EDX.

Conflict of interest

Author JH was employed by Diamond Light Source Ltd.

The remaining authors declare that the research was conducted in the absence of any commercial or financial relationships that could be construed as a potential conflict of interest.

Publisher's note

Supplementary material

The Supplementary Material for this article can be found online at: https://www.frontiersin.org/articles/10.3389/fenvc.2024.1445482/full#supplementary-material

References

Andriyko, L. S., Zarko, V., Gun'ko, V., Marynin, A., Olishevskiy, V., Skwarek, E., et al. (2015). Electrical and physical characteristics of silica nanoparticles in aqueous media affected by cations Na^+, Ba^{2+} and Al^{3+}. *Adsorpt. Sci. & Technol.* 33 (6-8), 601–607. doi:10.1260/0263-6174.33.6-8.601

Babu, C. M., Palanisamy, B., Sundaravel, B., Palanichamy, M., and Murugesan, V. (2013). A novel magnetic Fe_3O_4/SiO_2 core-shell nanorods for the removal of arsenic. *J. Nanosci. Nanotechnol.* 13 (4), 2517–2527. doi:10.1166/jnn.2013.7376

Basu, S. K., and McCutchan, E. A. (2020). Nuclear data sheets for A = 90. *Nucl. Data Sheets* 165, 1–329. doi:10.1016/j.nds.2020.04.001

Biswal, D., Peeples, B. N., Peeples, C., and Pradhan, A. K. (2013). Tuning of magnetic properties in cobalt ferrite by varying Fe^{+2} and Co^{+2} molar ratios. *J. Magnetism Magnetic Mater.* 345, 1–6. doi:10.1016/j.jmmm.2013.05.052

Browne, E., and Tuli, J. K. (2007). Nuclear data sheets for A = 137. *Nucl. Data Sheets* 108 (10), 2173–2318. doi:10.1016/j.nds.2007.09.002

Chandramohan, P., Srinivasan, M., Velmurugan, S., and Narasimhan, S. (2011). *Cation distribution and particle size effect on Raman spectrum of $CoFe_2O_4$*. *J. Solid State Chem.* 184 (1), 89–96. doi:10.1016/j.jssc.2010.10.019

Dang, F., Enomoto, N., Hojo, J., and Enpuku, K. (2010). Sonochemical coating of magnetite nanoparticles with silica. *Ultrason. Sonochemistry* 17 (1), 193–199. doi:10.1016/j.ultsonch.2009.05.013

Faghihian, H., Moayed, M., Firooz, A., and Iravani, M. (2014). Evaluation of a new magnetic zeolite composite for removal of Cs^+ and $Sr2^+$ from aqueous solutions: kinetic, equilibrium and thermodynamic studies. *Comptes Rendus Chim.* 17 (2), 108–117. doi:10.1016/j.crci.2013.02.006

Hijikata, T., Uozumi, K., Tsukada, T., Koyama, T., Ishikawa, K., Ono, S., et al. (2014). Early construction and operation of the highly contaminated water treatment system in Fukushima Daiichi Nuclear Power Station (II) – dynamic characteristics of KURION media for Cs removal in simulated contaminated water. *J. Nucl. Sci. Technol.* 51 (7-8), 894–905. doi:10.1080/00223131.2014.924885

INTERNATIONAL ATOMIC ENERGY AGENCY (2001). *Handling and processing of radioactive waste from nuclear applications*. Vienna: INTERNATIONAL ATOMIC ENERGY AGENCY.

Ito, A., Karmaoui, M., Thirunavukkarasu, G., and Hriljac, J. A. (2023). One-pot synthesis of superparamagnetically modified zeolite chabazite for removal of Cs^+ from radioactively contaminated water. *Apl. Mater.* 11 (4). doi:10.1063/5.0139282

Kubota, T., Fukutani, S., Ohta, T., and Mahara, Y. (2013). Removal of radioactive cesium, strontium, and iodine from natural waters using bentonite, zeolite, and activated carbon. *J. Radioanalytical Nucl. Chem.* 296 (2), 981–984. doi:10.1007/s10967-012-2068-4

Lemine, O. M., Omri, K., Zhang, B., El Mir, L., Sajieddine, M., Alyamani, A., et al. (2012). *Sol–gel synthesis of 8nm magnetite (Fe_3O_4) nanoparticles and their magnetic properties*. *Superlattices Microstruct.* 52 (4), 793–799. doi:10.1016/j.spmi.2012.07.009

Li, X.-H., Xu, C. L., Han, X. H., Qiao, L., Wang, T., and Li, F. S. (2010). Synthesis and magnetic properties of nearly monodisperse $CoFe_2O_4$ nanoparticles through a simple hydrothermal condition. *Nanoscale Res. Lett.* 5 (6), 1039–1044. doi:10.1007/s11671-010-9599-9

Lichvar, P., Rozloznik, M., and Sekely, S. (2013). *Behaviour of aluminosilicate inorganic matrix sial during and after solidification of radioactive sludge and radioactive spent resins and their mixtures*. International Atomic Energy Agency IAEA, 16.

Meisel, W. (1998). Degradation of materials and passivity. *Hyperfine Interact.* 111 (1), 59–70. doi:10.1023/a:1012676911360

Mimura, H., and Kanno, T. (1985). Distribution and fixation of cesium and strontium in zeolite A and chabazite. *J. Nucl. Sci. Technol.* 22 (4), 284–291. doi:10.3327/jnst.22.284

Munthali, M. W., Johan, E., Aono, H., and Matsue, N. (2015). Cs^+ and $Sr2^+$ adsorption selectivity of zeolites in relation to radioactive decontamination. *J. Asian Ceram. Soc.* 3 (3), 245–250. doi:10.1016/j.jascer.2015.04.002

Nishiyama, Y., Hanafusa, T., Yamashita, J., Yamamoto, Y., and Ono, T. (2016). Adsorption and removal of strontium in aqueous solution by synthetic hydroxyapatite. *J. Radioanalytical Nucl. Chem.* 307 (2), 1279–1285. doi:10.1007/s10967-015-4228-9

Oji, L. N., Martin, K. B., and Hobbs, D. T. (2009). Development of prototype titanate ion-exchange loaded-membranes for strontium, cesium and actinide decontamination from aqueous media. *J. Radioanalytical Nucl. Chem.* 279 (3), 847–854. doi:10.1007/s10967-008-7365-6

Pazik, R., Piasecka, E., Małecka, M., Kessler, V. G., Idzikowski, B., Śniadecki, Z., et al. (2013). Facile non-hydrolytic synthesis of highly water dispersible, surfactant free nanoparticles of synthetic MFe2O4 (M-Mn^{2+}, Fe^{2+}, Co_2+, Ni^{2+}) ferrite spinel by a modified Bradley reaction. *RSC Adv.* 3 (30), 12230–12243. doi:10.1039/c3ra40763b

Robson, H. (2001). *Verified synthesis of zeolitic materials*. Second Edition. Elsevier Science.

Smart, L. E., and Moore, E. A. (2012). *Solid state chemistry: an introduction*. Boca Raton: CRC Press.

Stöber, W., Fink, A., and Bohn, E. (1968). Controlled growth of monodisperse silica spheres in the micron size range. *J. Colloid Interface Sci.* 26 (1), 62–69. doi:10.1016/0021-9797(68)90272-5

Sugihara, T. T., James, H. I., Troianello, E. J., and Bowen, V. T. (1959). Radiochemical separation of fission products from large volumes of sea water. Strontium, cesium, cerium, and promethium. *Anal. Chem.* 31 (1), 44–49. doi:10.1021/ac60145a009

Tan, C. G., Bowen, B. D., and Epstein, N. (1987). Production of monodisperse colloidal silica spheres: effect of temperature. *J. Colloid Interface Sci.* 118 (1), 290–293. doi:10.1016/0021-9797(87)90458-9

Umut, E., Coşkun, M., Güngüneş, H., Dupuis, V., and Kamzin, A. S. (2021). *Spin Canting in silica-coated nickel ferrite ($NiFe_2O_4@SiO_2$) nanoparticles: a mössbauer spectroscopy study*. *J. Supercond. Nov. Magnetism* 34 (3), 913–924. doi:10.1007/s10948-020-05800-y

Yáñez-Vilar, S., Sánchez-Andújar, M., Gómez-Aguirre, C., Mira, J., Señarís-Rodríguez, M., and Castro-García, S. (2009). A simple solvothermal synthesis of MFe_2O_4 (M=Mn, Co and Ni) nanoparticles. *J. Solid State Chem.* 182 (10), 2685–2690. doi:10.1016/j.jssc.2009.07.028